The HERMES polarized hydrogen and deuterium gas target in the HERA electron storage ring

A. Airapetian[a], N. Akopov[b], Z. Akopov[b], M. Amarian[b,c], A. Andrus[d], E.C. Aschenauer[c,*], W. Augustyniak[e], R. Avakian[b], A. Avetissian[b], E. Avetissian[f], P. Bailey[d], D. Balin[g], C. Baumgarten[h,1], M. Beckmann[i], S. Belostotski[g], N. Bianchi[f], H.P. Blok[j,k], H. Böttcher[c], A. Borissov[l], A. Borysenko[f], M. Bouwhuis[d], B. Braun[m], A. Brüll[n], V. Bryzgalov[o], G.P. Capitani[f], M. Capiluppi[p], T. Chen[q], G. Ciullo[p], M. Contalbrigo[p], G. Court[r], P.F. Dalpiaz[p], R. De Leo[s], M. Demey[j], L. De Nardo[t], E. De Sanctis[f], E. Devitsin[u], P. Di Nezza[f], M. Düren[v], M. Ehrenfried[m], A. Elalaoui-Moulay[w], G. Elbakian[b], F. Ellinghaus[c], U. Elschenbroich[x], R. Fabbri[j], A. Fantoni[f], A. Fechtchenko[y], L. Felawka[z], S. Frullani[aa], G. Gapienko[o], V. Gapienko[o], F. Garibaldi[aa], K. Garrow[z], G. Gavrilov[i,z], V. Gharibyan[b], G. Graw[h], O. Grebeniouk[g], I.M. Gregor[c], C. Hadjidakis[f], W. Haeberli[ab], K. Hafidi[w], M. Hartig[v], D. Hasch[f], D. Heesbeen[j], M. Henoch[m], R. Hertenberger[h], W.H.A. Hesselink[j,k], A. Hillenbrand[m], M. Hoek[v], Y. Holler[i], B. Hommez[x], I. Hristova[c], G. Iarygin[y], A. Ivanilov[o], A. Izotov[g], H.E. Jackson[w], A. Jgoun[g], R. Kaiser[l], E. Kinney[ac], A. Kisselev[ac], T. Kobayashi[ad], N. Koch[m,2], H. Kolster[h,k,3], M. Kopytin[c], V. Korotkov[o], V. Kozlov[u], B. Krauss[m], V.G. Krivokhijine[y], L. Lagamba[s], L. Lapikás[j], A. Laziev[j,k], P. Lenisa[p,f,*], P. Liebing[c], L.A. Linden-Levy[d], W. Lorenzon[a], H. Lu[ae], J. Lu[z], S. Lu[v], B.-Q. Ma[q], B. Maiheu[x], N.C.R. Makins[d], Y. Mao[q], B. Marianski[e], H. Marukyan[b], V. Mexner[j], N. Meyners[i], R. Mussa[p], O. Mikloukho[g], C.A. Miller[t,z], Y. Miyachi[ad], V. Muccifora[f], A. Nagaitsev[y], E. Nappi[s], Y. Naryshkin[g], A. Nass[m], M. Negodaev[c], W.-D. Nowak[c], K. Oganessyan[i,f], H. Ohsuga[ad], A. Osborne[l], N. Pickert[m], D.H. Potterveld[w], M. Raithel[m], D. Reggiani[p], P.E. Reimer[w], A. Reischl[j], A.R. Reolon[f], C. Riedl[m], K. Rith[m], G. Rosner[l], A. Rostomyan[b], L. Rubacek[v], J. Rubin[d], D. Ryckbosch[x], Y. Salomatin[o], I. Sanjiev[w,g], I. Savin[y], C. Schill[f],

*Corresponding authors.
  E-mail addresses: Aschenauer@mail.desy.de (E.C. Aschenauer), lenisa@mail.desy.de (P. Lenisa).

G. Schnell[c], K.P. Schüler[i], J. Seele[d], R. Seidl[m], B. Seitz[v], R. Shanidze[m],
C. Shearer[l], T.-A. Shibata[ad], V. Shutov[y], K. Sinram[i], W. Sommer[v], M. Stancari[p],
M. Statera[p], E. Steffens[m], J.J.M. Steijger[j], H. Stenzel[v], J. Stewart[c], F. Stinzing[m],
P. Tait[m], H. Tanaka[ad], S. Taroian[b], B. Tchuiko[o], A. Terkulov[u], A. Trzcinski[e],
M. Tytgat[x], A. Vandenbroucke[x], P. van der Nat[j], G. van der Steenhoven[j], Y. van
Haarlem[x], M.C. Vetterli[af,z], V. Vikhrov[g], M.G. Vincter[t], C. Vogel[m],
J. Volmer[c], S. Wang[ae], J. Wendland[af,z], J. Wilbert[m], T. Wise[ab], G. Ybeles Smit[k],
Y. Ye[ae], Z. Ye[ae], S. Yen[z], B. Zihlmann[x], P. Zupranski[e]

[a]*Randall Laboratory of Physics, University of Michigan, Ann Arbor, MI 48109-1120, USA*
[b]*Yerevan Physics Institute, 375036 Yerevan, Armenia*
[c]*DESY, Platanenallee 6, 15738 Zeuthen, Germany*
[d]*Department of Physics, University of Illinois, Urbana, IL 61801-3080, USA*
[e]*Andrzej Soltan Institute for Nuclear Studies, 00-689 Warsaw, Poland*
[f]*Istituto Nazionale di Fisica Nucleare, Laboratori Nazionali di Frascati, 00044 Frascati, Italy*
[g]*Petersburg Nuclear Physics Institute, St. Petersburg, Gatchina 188350, Russia*
[h]*Sektion Physik, Universität München, 85748 Garching, Germany*
[i]*DESY, 22603 Hamburg, Germany*
[j]*Nationaal Instituut voor Kernfysica en Hoge-Energiefysica (NIKHEF), 1009 DB Amsterdam, The Netherlands*
[k]*Department of Physics and Astronomy, Vrije Universiteit, 1081 HV Amsterdam, The Netherlands*
[l]*Department of Physics and Astronomy, University of Glasgow, Glasgow G12 8QQ, UK*
[m]*Physikalisches Institut, Universität Erlangen-Nürnberg, 91058 Erlangen, Germany*
[n]*Laboratory for Nuclear Science, Massachusetts Institute of Technology, Cambridge, MA 02139, USA*
[o]*Institute for High Energy Physics, Protvino, Moscow region, 142281 Russia*
[p]*Istituto Nazionale di Fisica Nucleare, Sezione di Ferrara and Dipartimento di Fisica, Università di Ferrara, 44100 Ferrara, Italy*
[q]*School of Physics, Peking University, Beijing 100871, China*
[r]*Physics Department, University of Liverpool, Liverpool L69 7ZE, UK*
[s]*Istituto Nazionale di Fisica Nucleare, Sezione di Bari, 70124 Bari, Italy*
[t]*Department of Physics, University of Alberta, Edmonton, Alberta T6G 2J1, Canada*
[u]*Lebedev Physical Institute, 117924 Moscow, Russia*
[v]*Physikalisches Institut, Universität Gießen, 35392 Gießen, Germany*
[w]*Physics Division, Argonne National Laboratory, Argonne, IL 60439-4843, USA*
[x]*Department of Subatomic and Radiation Physics, University of Gent, 9000 Gent, Belgium*
[y]*Joint Institute for Nuclear Research, 141980 Dubna, Russia*
[z]*TRIUMF, Vancouver, British Columbia V6T 2A3, Canada*
[aa]*Istituto Nazionale di Fisica Nucleare, Sezione Roma 1, Gruppo Sanità and Physics Laboratory,
Istituto Superiore di Sanità, 00161 Roma, Italy*
[ab]*Department of Physics, University of Wisconsin-Madison, Madison, WI 53706, USA*
[ac]*Nuclear Physics Laboratory, University of Colorado, Boulder, CO 80309-0446, USA*
[ad]*Department of Physics, Tokyo Institute of Technology, Tokyo 152, Japan*
[ae]*Department of Modern Physics, University of Science and Technology of China, Hefei, Anhui 230026, China*
[af]*Department of Physics, Simon Fraser University, Burnaby, British Columbia V5A 1S6, Canada*

[1]Current address: ACCEL Instruments GmbH, Friedrich-Ebert-Str. 1, D-51429 Bergisch Gladbach, Germany
[2]Current address: Thales Electron Devices GmbH, Söflinger Str. 100, 89077 Ulm, Germany
[3]Current address: Laboratory for Nuclear Science, Massachusetts Institute of Technology, Cambridge, MA 02139, USA

Abstract

The HERMES hydrogen and deuterium nuclear-polarized gas targets have been in use since 1996 with the polarized electron beam of HERA at DESY to study the spin structure of the nucleon. Polarized atoms from a Stern–Gerlach Atomic Beam Source are injected into a storage cell internal to the HERA electron ring. Atoms diffusing from the center of the storage cell into a side tube are analyzed to determine the atomic fraction and the atomic polarizations. The atoms have a nuclear polarization, the axis of which is defined by an external magnetic holding field. The holding field was longitudinal during 1996–2000, and was changed to transverse in 2001. The design of the target is described, the method for analyzing the target polarization is outlined, and the performance of the target in the various running periods is presented.

1. Introduction

The HERMES experiment at HERA (DESY, Hamburg) was designed to study the quark-gluon spin structure of the nucleon by deeply inelastic scattering (DIS) of longitudinally polarized electrons from a polarized gas target of hydrogen and deuterium atoms internal to a storage ring [1,2]. The 27.5 GeV electron beam stored in the HERA storage ring with currents up to 50 mA is polarized by the Sokolov–Ternov effect [3], with a time constant of about 30 min. A longitudinal spin direction is obtained where the experiment is located within the HERA east straight section by means of a pair of spin rotators [4]. In a machine with one pair of spin rotators before the 2001 upgrade, a typical polarization of 60% was achieved.

The HERMES experiment [5] was proposed in 1990, and is designed to run in parallel with the ZEUS and H1 collider experiments without significantly reducing the electron beam lifetime, which is of the order of 10 h. This limits the target areal density to about 10^{15} H-atoms/cm^2 and excludes the use of any solid target material. A target employing a cold storage cell fed by a a polarized atomic beam source was proposed and implemented. Polarized gas targets for storage rings were reviewed recently by Steffens and Haeberli [6].

Since 1996, the present target apparatus for polarized hydrogen and deuterium has been in operation. During the years 1996–97 longitudinally polarized hydrogen H$_{||}$ was used, while longitudinally polarized deuterium was employed in 1998–2000 (D$_{||}$), and from 2002 onwards, transversely polarized hydrogen (H$_{\perp}$) has been in use.

Apart from a high areal density and reliable operation over many years, the most challenging requirement for the internal target was to determine the effective target polarization seen by the beam. The target polarization cannot be measured by making use of scattering processes involving the high-energy electron beam due to the small cross-sections involved. Nuclear vector polarization P_z and, for deuterium also the tensor polarization P_{zz} were to be measured, as well as the electron polarization P_e for diagnostic purposes. The required accuracy was $\delta P = 0.03$ absolute uncertainty on the average polarization over long measuring periods, and 1% statistical accuracy within a couple of minutes in order to monitor possible changes in time. This goal was achieved by employing a sampling technique in conjunction with detailed simulations and frequent calibration measurements.

In the present article, an overview of the HERMES polarized hydrogen and deuterium gas target is given with reference to the various papers

describing the subsystems of the target. The atomic beam source (ABS) [7], the storage cell [8], the Target Gas Analyzer (TGA) [9] and the Breit–Rabi polarimeter (BRP) [10] are summarized in Section 2. Section 3 describes the analysis applied to the raw TGA and BRP signals and the several calibrations required to derive measured values for the degree of dissociation and the atomic polarizations of the sample gas.[1] Section 4 reviews the various physical processes inside the storage cell that directly influence the TGA and BRP analyses [11–14]. The results of the target analysis are reported in Sections 6 and 7. Section 8 mentions a selection of measurements carried out by HERMES that crucially depended on the polarized target. The paper is concluded in Section 9.

2. Survey of experimental apparatus

The HERMES polarized hydrogen and deuterium target, schematically shown in Fig. 1, consists of an atomic beam source (ABS) that injects a spin polarized beam of H or D atoms into a thin-walled storage cell. A sample of gas diffuses from the center of the cell into a Breit Rabi Polarimeter (BRP) that measures the atomic polarizations, or into a Target Gas Analyzer (TGA) that measures the relative atomic and molecular content of the gas. A magnet surrounding the storage cell provides a holding field defining the polarization axis and preventing spin relaxation by effectively decoupling the magnetic moments of electrons and nucleons.

2.1. Target chamber

The target chamber shown in Fig. 2 is evacuated by two turbo-molecular pumps with a combined speed of $4400 \, \text{s}^{-1}$. During operation the chamber pressure is typically in the 10^{-7} mbar range due to the high gas load from the atomic beam, which enters the chamber from $30°$ above the horizontal plane. The storage cell and its supporting cooling rails are cantilevered from the upstream[2] end flange.

A 0.3 mm thick stainless steel exit window on the downstream end of the target chamber allows the scattered electrons and hadronic fragments to leave the target chamber and to be detected by the HERMES spectrometer [5]. This thin window is integral with the following thin-walled beam tube with no intervening flange, in order to minimize the high-Z material in this region and reduce shower production by π^0 mesons produced at small angles. About 1 m upstream of the target cell, an adjustable collimator (labeled C1) is located to stop direct synchrotron radiation. It normally has the smallest scaled aperture in the HERA ring, and is opened during electron injection [5]. A fixed collimator (labeled C2) just upstream of the storage cell protects it from synchrotron light scattered by C1 and from exposure to electron showers from C1.

For longitudinal running the storage cell and vacuum chamber are immersed in a longitudinal field generated by a superconducting magnet. The magnet consists of four coils and an iron yoke designed to provide optimum field uniformity over the length of the storage cell while providing a central gap for the atomic beam to enter the cell. The magnetic field (up to 350 mT) provides the quantization axis for the spins of the polarized atoms in the storage cell, and decouples the spins of the nucleons and electrons. The passing HERA beam is bunched to provide high luminosity for the collider experiments H1 and ZEUS. As discussed in Section 4.2.4, this may induce resonant nuclear depolarization of the target gas. The induced resonances can be avoided by proper setting of the holding field, provided that its homogeneity is sufficient [12]. In the case of hydrogen, the maximum permissible variation of the magnetic field along the storage cell is 1.5%. For operating with deuterium gas, this requirement was found to be less critical [15].

---

[1]In this article, the term ''atomic polarizations'' refers to the polarizations of the electrons and nuclei in the atoms.

[2]Upstream and downstream mean with respect to the HERA lepton beam direction.
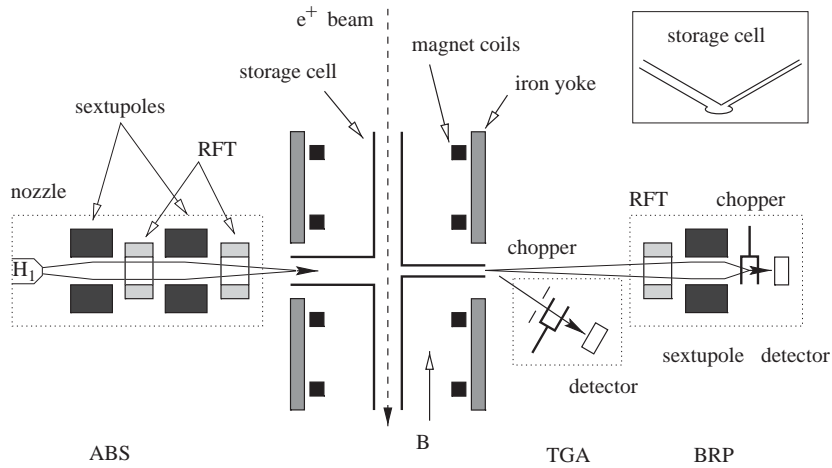
Fig. 1. Schematic view of the HERMES longitudinally polarized target. From left to right: atomic beam source (ABS), target chamber with cell and magnet, and diagnostic system composed by Target Gas Analyzer (TGA) and Breit–Rabi polarimeter (BRP). The locations of the radio-frequency transition (RFT) units are indicated.
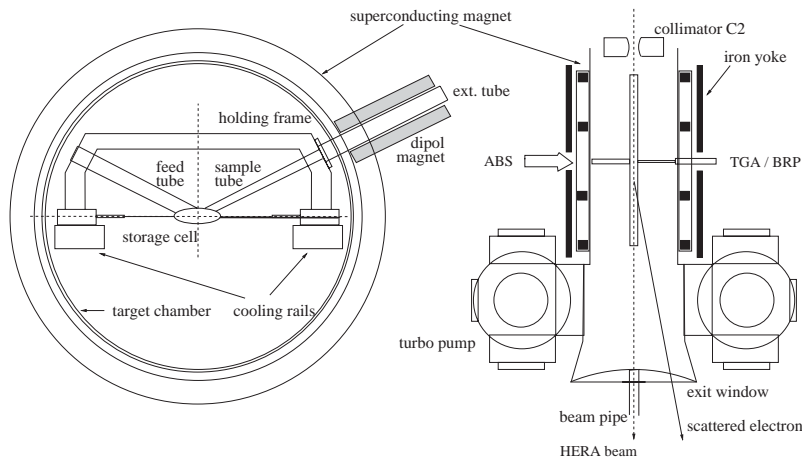
Fig. 2. Longitudinal target chamber and superconducting magnet viewed from downstream with respect to the HERA beam direction (left), and from above (right).

2.2. Transverse magnet

After the end of the longitudinal running in 2000, the HERMES target was modified for measurements with a hydrogen gas target in a transversely oriented magnetic holding field. The intensity of the transverse magnetic field was limited by the amount of synchrotron radiation power generated by the deflection of the beam by the target magnet (5 kW maximum), so it was

decided to build a normal conducting magnet. As will be explained in Section 4.2.4, a better homogeneity of the transverse target magnet of $\Delta B \leqslant 0.15\,\text{mT}$ at a field value of about 300 mT was required.

The geometrical constraints imposed by the HERMES acceptance made it difficult to design a magnet fulfilling the uniformity requirement. After construction, the field uniformity was measured and improved by shimming the pole tips. At a field

strength of $B = 297$ mT, maximum deviations of $\Delta B_z = 0.05$ mT, $\Delta B_y = 0.15$ mT and $\Delta B_x = 0.60$ mT within the storage cell volume have been achieved, z being the longitudinal direction, y the vertical and x the horizontal axis. The magnet was installed in July 2001. The strength of the transverse field vs. z is shown in the lower plot of Fig. 3.

2.3. The storage cell

The HERMES storage cell [8] is made of two 75 μm thin pure aluminum sheets, which are tightly spot-welded together. It is 400 mm long and has an elliptical cross-sectioned shape of 21×8.9 mm^2. All the aluminum parts of the cell are coated with Drifilm [16] to minimize gas depolar-

Fig. 3. Upper panel: field strength of the longitudinal target magnet measured along the HERA beam direction z, covering the full length of the storage cell. The line shows a polynomial fit to the measurement. Lower panel: transverse magnet field uniformity measured along the z axis at the nominal field strength $B = 297$ mT. Deviations of $\Delta B_y = 0.15$ mT (vert.) and $\Delta B_x = 0.60$ mT (horiz.) have been measured within the cell volume.

ization and recombination caused by wall collisions [17–20]. A vented extension of the cell continues about 147 mm downstream of the cell before joining the thicker-walled wakefield-suppressing transition tube, to ensure that all scattered particles inside the spectrometer detector acceptance pass through the minimum thickness of material (see Fig. 4). The wake field suppressors are made of 100 μm thick titanium, and confine the electromagnetic high frequency field of the bunched HERA beam, forming a gradual electrical transition between the storage cell and the HERA beam pipe.

Cells with three different elliptical cross-sections have been used thus far. The mentioned size of 21×8.9 mm^2 is the one in use since December 1999, called the medium-sized cell. The largest was used until December 1999, and had a cross-section of 29×9.8 mm^2. (A small one (19×8.0 mm^2) was tested in January 1999 and found to be too small.) Table 1 summarizes dimensions and conductances of the three cells that have been used. The conductance values apply to gas injected into the cell center.

The storage cell is mounted onto cooling rails, which are cooled by temperature regulated gaseous helium. The optimum operating temperature for hydrogen targets was found to be about 100 K, where recombination and depolarization effects are low. Additionally, the lower conductance at this temperature leads to a higher target thickness by a factor $\sqrt{3}$ compared to room temperature. For deuterium gas the target temperature could be decreased further to about 65 K, which increased the target thickness by about 23 % compared to 100 K.

The temperature of the cooling rails is monitored at three locations by platinum resistors. Since 1999 an additional thermocouple wire has been attached to the aluminum foil close to the cell ellipse to directly monitor the cell temperature during injection of the HERA beam when a temperature rise of about 5–10 K is usually detected. The cooling rails are mounted on the target chamber flange on the upstream end. Due to thermal contraction of the cell when being cooled, the position of the cell center changes relative to the atomic beam source and the Breit–Rabi
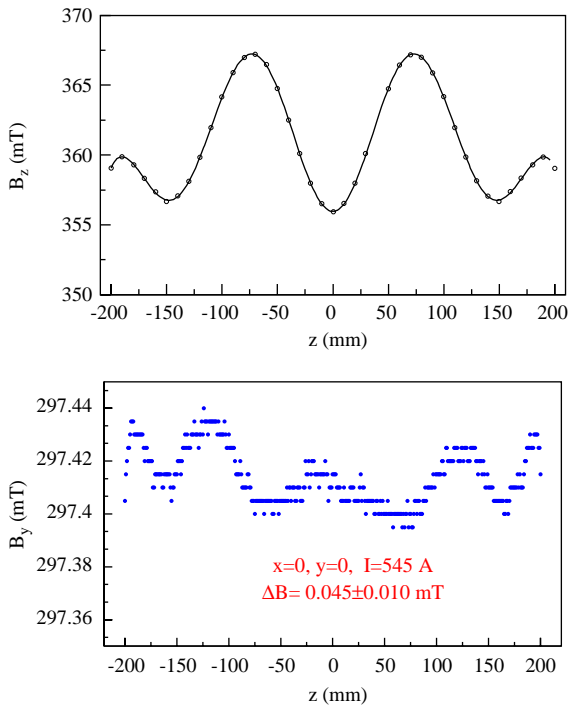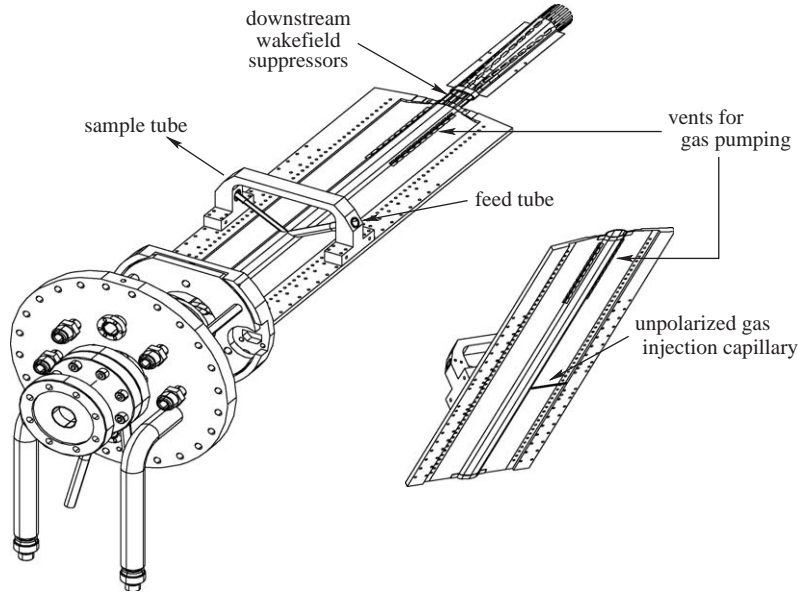
Fig. 4. The storage cell and its support flange.

Table 1
The history of cells used by HERMES

Period of use	Cross-section $a \times b$ (mm)	Conductance (l/s)
05.96–11.99	29.8×9.8	$1.45\sqrt{T/M}$
01.99 (test)	19.8×8.0	$0.61\sqrt{T/M}$
12.99–now	21.0×8.9	$0.80\sqrt{T/M}$

The lengths of the major and minor axes of the ellipse are indicated by a and b; T is the temperature of the cell in K, and M is the atomic mass of the gas in amu.

polarimeter. From room temperature down to 100 K the cell center moves by 0.9 mm. The alignment of the atomic beam source and Breit–Rabi polarimeter relative to the cell center includes an offset to compensate for this effect at the target operating temperature.

The cell is shown along with its support flange in Fig. 4. Two side tubes are connected to the beam tube, one to inject the polarized atoms and another smaller one to sample about 5% of the target gas and analyze it in the target gas analyzer and the Breit–Rabi polarimeter. The sample tube is tilted by 120° with respect to the axis of the injection

tube to ensure that the sampled atoms have thermalized with the storage cell wall. A permanent dipole magnet around the sampling tube outside the target chamber extends the magnetic holding field of the target magnet to prevent depolarization (see Fig. 2). A capillary near the location of the feed tube allows injection of unpolarized gas into the cell.

2.4. Atomic beam source

The atomic beam source [7] consists of a dissociator, a powerful differential pumping system, a beam forming system, a sextupole magnet system to focus atoms with $m_S = +\frac{1}{2}$ into the storage cell, and adiabatic high-frequency transitions to manipulate the hyperfine population of the atomic beam. Injected fluxes of $\Phi^{ABS} \approx 6.5 \times 10^{16}$ atoms/s in the case of hydrogen (2 states) and $\Phi^{ABS} \approx 4.5 \times 10^{16}$ atoms/s in the case of deuterium (3 states) have been observed. These values are calculated from the density-dependent spin exchange relaxation [15]. The injected nuclear polarization P_z^{inj} was constantly above 0.97 for hydrogen and above 0.91 for deuterium.

A schematic diagram of the ABS is depicted in Figs. 5 and 6.

Molecular hydrogen/deuterium gas enters the dissociator from the left. The molecules are dissociated by a radio frequency discharge with a frequency of 13.56 MHz in a pyrex tube, producing a degree of dissociation up to 80 % (H_2, D_2) at a flow of about $1\,mbar\,1s^{-1}$ and a radio frequency power of 300 W. To maximize the stability and the degree of dissociation, an amount of oxygen between 0.1 and 0.3 volume percent is added to the molecular gas.

A high degree of dissociation at higher flow can potentially be achieved using a recently developed microwave (MW) dissociator [21], which operates at a frequency of 2.45 GHz. With typical flows between 1 and $2\,mbar\,1s^{-1}$ and a microwave power of about 600 W, a degree of dissociation higher than 80 % is achieved. The MW dissociator was used in the year 2000 when running with deuterium, when it provided a target thickness improvement of 5–10 %. The RF dissociator has been used since, because the ABS sextupole system is not optimized for the lower atomic velocity distribution produced by the MW dissociator, eliminating the possible benefit for hydrogen.

The atomic gas flows through a conical nozzle with an opening diameter of 2 mm, which is cooled to about 100 K. The water produced in the discharge freezes in the nozzle. Although this beneficially reduces surface recombination, the ice layer continuously thickens and slowly reduces the
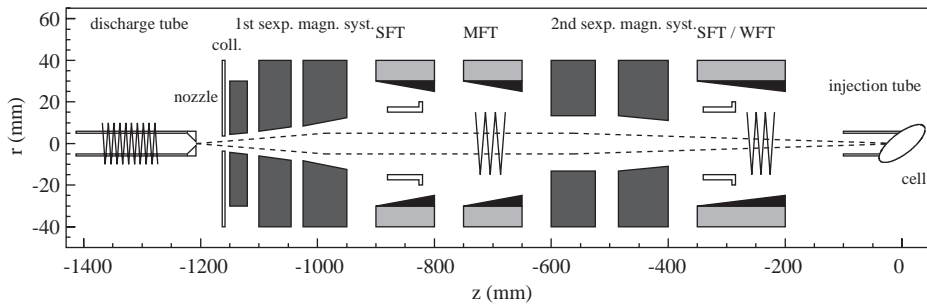
Fig. 5. Schematic view (from downstream of the electron beam) of the HERMES ABS with dissociator and collimator for beam formation. Two sets of sextupole magnets are located along the beam axis as are the high-frequency transitions. The axis of the ABS is tilted by 30° downwards with respect to the horizontal plane.

Fig. 6. Hyperfine energy levels of hydrogen (left) and deuterium (right) atoms as a function of the magnetic holding field (Breit–Rabi diagram) and corresponding labeling. The field values are scaled with the corresponding critical field and energy values with the corresponding hyperfine energy.

Table 2
Injection modes of the atomic beam source

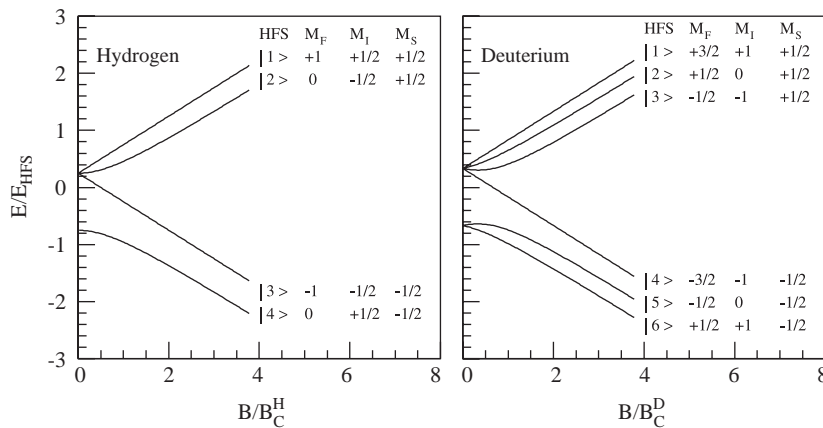| Gas	HFT (betw. 6-poles)	HFT (after 6-poles)	Inj. states	P_e	P_z	P_{zz}	Use
H	—	—	$\lvert 1\rangle$, $\lvert 2\rangle$	$+1$	0	—	Cal
	—	WFT 1–3	$\lvert 2\rangle$, $\lvert 3\rangle$	0	-1	—	Data
	—	SFT 2–4	$\lvert 1\rangle$, $\lvert 4\rangle$	0	$+1$	—	Data
	SFT 2–4 / MFT 2–3	—	$\lvert 1\rangle$	$+1$	$+1$	—	Cal
	WFT 1–3/MFT 1–3	—	$\lvert 2\rangle$	$+1$	-1	—	Cal
	SFT 2–4 / MFT 2–3	WFT 1–3	$\lvert 3\rangle$	-1	-1	—	Cal
	WFT 1–3 / MFT 1–3	SFT 2–4	$\lvert 4\rangle$	-1	$+1$	—	Cal
	WFT 1–3, SFT 2–4	—	*no state*	—	—	—	Cal
D	—	—	$\lvert 1\rangle\ \lvert 2\rangle\ \lvert 3\rangle$	$+1$	0	0	Cal
	SFT 2–5	WFT 1–4	$\lvert 3\rangle\ \lvert 4\rangle$	0	-1	$+1$	Data
	SFT 3–5	SFT 2–6	$\lvert 1\rangle\ \lvert 6\rangle$	0	$+1$	$+1$	Data
	MFT 1–4	SFT 3–5	$\lvert 2\rangle\ \lvert 5\rangle$	0	0	-2	Data
	MFT 1–4	SFT 2–6	$\lvert 3\rangle\ \lvert 6\rangle$	0	0	$+1$	Data
	MFT 3–4, SFT 2–6	—	$\lvert 1\rangle$	$+1$	$+1$	$+1$	Cal
	WFT 1–4, SFT 2–6	—	$\lvert 2\rangle$	$+1$	0	-2	Cal
	WFT 1–4, SFT 3–5	—	$\lvert 3\rangle$	$+1$	-1	$+1$	Cal
	MFT 3–4, SFT 2–6	WFT 1–4	$\lvert 4\rangle$	-1	-1	$+1$	Cal
	WFT 1–4, SFT 3–5	SFT 3–5	$\lvert 5\rangle$	$+1$	0	-2	Cal
	WFT 1–4, SFT 2–6	SFT 2–6	$\lvert 6\rangle$	-1	$+1$	$+1$	Cal

The table shows the high frequency transition (HFT) units employed (2nd and 3rd columns), the hyperfine states injected in the target cell and the resulting electron (P_e), nuclear (P_z) and tensor (P_{zz}) polarizations in the ideal case of 100 % efficiency of the sextupole system and transition units, no depolarization inside the target cell and infinitely strong guide field. The last column clarifies the purpose of each mode (Cal: calibration, monitoring; Data: normal HERMES operation). The injection modes for hydrogen and deuterium single states are listed separately. For some modes the MFT between the sextupoles has to be tuned as a WFT 1–4. The *no state* injection mode is possible only for hydrogen and has been operational since April 2002. The adopted labeling for the hyperfine states is explained in the Breit–Rabi diagram of Fig. 6.

gas conductance of the nozzle. After typically 3–5 days of operation, the pressure in the dissociator tube rises substantially, increasing volume recombination in the tube and resulting in a noticeable decrease in the degree of dissociation of gas exiting the nozzle. Full recovery is achieved by slightly warming up the nozzle to remove the ice layer.

After passing the cold nozzle, the gas expands into the vacuum of the dissociator chamber. A powerful differential pumping system with a total nominal pumping speed of more than $15{,}000\,\mathrm{s}^{-1}$ suppresses scattering of the atomic beam, and ensures low gas flow into the HERA vacuum system.

The magnet system of the HERMES atomic beam source consists of a total of five Halbach type [22] segmented permanent sextupole magnets with a maximum poletip field of about 1.5 T. Every magnet consists of 24 segments of *Vacodym*

alloy.[3] Four high-frequency transition units are available: two between the sextupole magnets and two after the last magnet. The system provides enough flexibility that many different combinations of hyperfine states can be injected into the cell. Between the sextupoles, a strong field transition (SFT) and a medium field transition (MFT) can be used simultaneously, whereas the weak field transition (WFT) and the SFT after the sextupole magnets can only be used separately, because they share the coils for the static and gradient magnetic fields. The complete set of possible hyperfine populations that can be produced is shown in Table 2.

---

[3]Vacodym is a registered trademark of Vacuumschmelze GmbH, Hanau, Germany.

2.5. Target gas analyzer

The target gas analyzer (TGA) [9] measures the atomic and molecular content of the gas extracted from the storage cell through the sample tube. The TGA arrangement, shown in Fig. 7, consists of a pair of baffles, a chopper, a 90° off-axis quadrupole mass spectrometer (QMS) with a cross-beam ionizer and a channel electron multiplier (CEM) for single ion detection. The TGA is integrated into the vacuum system of the BRP sextupole chamber, which is served by two cryopumps and a titanium sublimation pump, with a total pumping speed of about $7000\,1\,s^{-1}$. During operation, the pressure in the TGA detector is about $4 \cdot 10^{-9}$ mbar. Prior to normal operation, the TGA vacuum chamber is baked with temperatures up to 180°C for 48 h. The BRP/TGA vacuum scheme is shown in Fig. 8.

The TGA is mounted 7° off-axis with respect to the BRP, in order not to interfere with the beam entering the polarimeter. The first baffle ensures that only gas from the sample beam can reach the detector, while the second one acts as a collimator, so that no atoms can hit the metal parts of the ionizer and recombine. The chopper, placed between the two baffles, rotates at a frequency of 5.5 Hz, thus periodically blocking the sample beam in order to allow subtraction of the residual gas signal. Particles entering the detector are ionized by 70 eV electrons, mass filtered with the QMS, and finally detected by the CEM. The pulses are counted by a 2048-bin time-resolving counter (TRC). The bin length is typically set to 175 μs
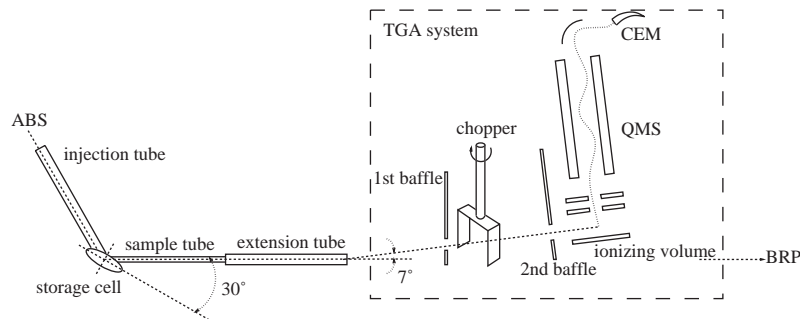

Fig. 7. A schematic diagram of the Target Gas Analyzer. The gas of atoms and molecules diffuses through the extension tube and is collimated by two baffles before entering the ionizing volume. The chopper is used for background subtraction.
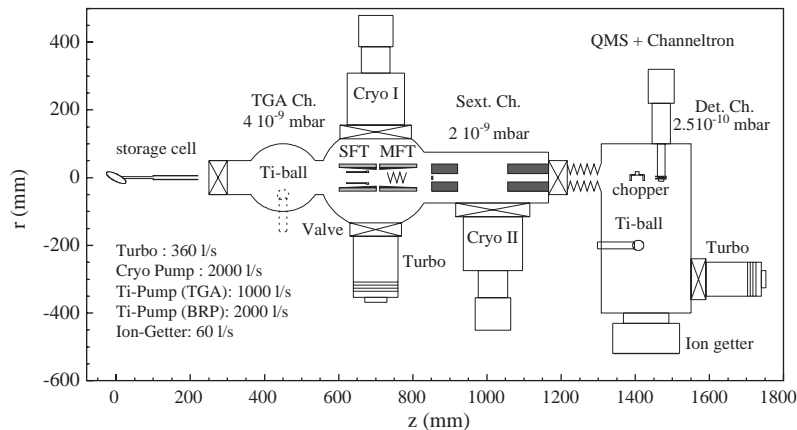

Fig. 8. Schematic view of the BRP/TGA vacuum system.

so that two chopper turns are collected within the whole bin range as shown in Fig. 9. The synchronization between chopper status and counting rate is given by a trigger signal coming from the chopper motor. The beam rate is calculated by taking the difference between the number of counts collected with the chopper open and closed.

2.6. Breit–Rabi polarimeter

The Breit–Rabi polarimeter (BRP) [10] measures the relative populations n_i of the hyperfine states of hydrogen (or deuterium) atoms contained in the sample beam. From this measurement, the absolute atomic polarizations can be calculated by applying the knowledge of the target magnetic field strength.

A schematic view of the BRP is shown in Fig. 10. From left to right, the sample beam leaves the extension tube of the target cell, encountering first two hyperfine transition units, then a sextuple magnet system and eventually the detector stage. During operation, a differential pumping system keeps the pressure at 2×10^{-9} mbar in the sextupole chamber and at 2.5×10^{-10} mbar in the detector chamber.

Two transition units are used to exchange the populations between pairs of hyperfine states: a strong field transition unit (SFT) with tilted resonator that can be tuned for both π and σ transitions, and a medium field transition (MFT)
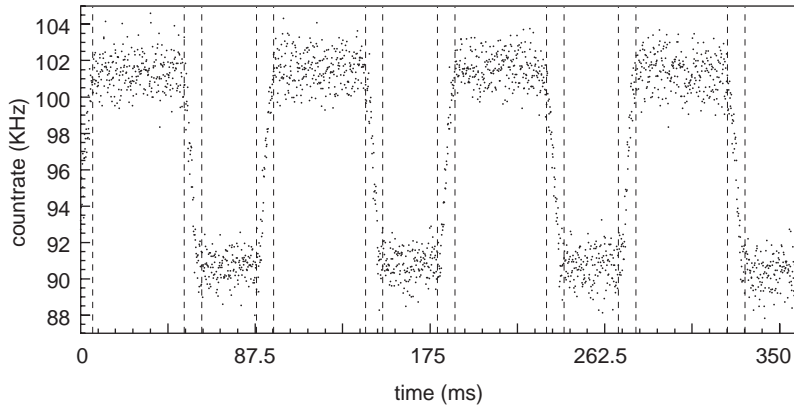
Fig. 9. Time spectrum of atomic count rates in the TGA. The vertical lines indicate the binning used to define the chopper positions open, undefined and closed.
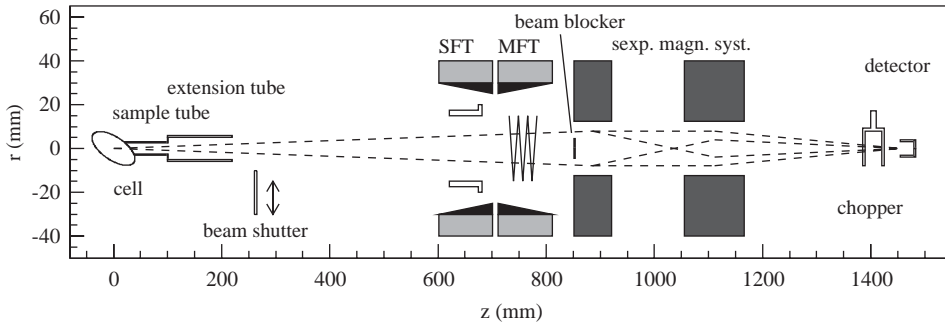
Fig. 10. Schematic layout of the BRP. The RF-transition units extend from $z = 600$ to 810 mm. The beam blocker at the entrance to the first 6-pole magnet ensures 100 % rejection of atoms with $m_s = -\frac{1}{2}$. The beam shutter is used to measure the hydrogen contribution coming from dissociative water ionization.

unit that can induce various π transitions according to the static field strength and gradient setting used. The sextupole system is composed of two magnets which focus the atoms of the sample beam with $m_s = +\frac{1}{2}$ towards the BRP geometrical axis and defocus the ones with $m_s = -\frac{1}{2}$. A 9 mm diameter beam blocker placed in front of the first sextupole magnet ensures that no atoms in $m_s = -\frac{1}{2}$ states can reach the detector. The sextupole system was redesigned in the year 2000 in order to improve the transmission probability at the typical cell temperature. The detector stage is identical to the one employed for the target gas analyzer: a cross-beam ionizer, a quadrupole mass spectrometer (QMS) and a channel electron multiplier (CEM). In contrast to the TGA, only hydrogen (or deuterium) *atoms* are detected by the BRP. The chamber residual gas correction is carried out by using a chopper in the same way as described for the TGA. An additional beam shutter is placed just after the extension tube exit to measure the possible contribution of atomic hydrogen coming from the dissociation of H_2O and H_2 (D_2O, DHO, D_2 and DH in the deuterium case) present on the vacuum chamber walls.[4]

3. Analysis of TGA and BRP signals

3.1. Interpretation of the TGA signals

The measured TGA atomic (molecular) signal S_a (S_m) is proportional to the product of the *particle* flux Φ_a (Φ_m) into the TGA, the mean inverse velocity of the particles $\langle\frac{1}{v_a}\rangle$ ($\langle\frac{1}{v_m}\rangle$), the ionization cross-section σ_a^{ion} (σ_m^{ion}) and the detection probability ε_a (ε_m). A dependence of the signal on the emission current is measured and taken into account by the normalization function $f(I_{emiss})$. Taking all parameters into account one finds:

$$S_{a,m} \propto f(I_{emiss})\sigma_{a,m}^{ion}\varepsilon_{a,m}\left\langle\frac{1}{v_{a,m}}\right\rangle\Phi_{a,m}. \qquad (1)$$

The total flux Φ^{TGA} of H or D nucleons into the TGA can be related to the particle fluxes Φ_a and Φ_m by

$$\Phi^{TGA} = \Phi_a + 2\Phi_m. \qquad (2)$$

The TGA geometrical acceptance is such that detected particles have bounced typically more than 100 times on the extension tube inner surface [15]. For this reason, particles entering the TGA detector have thermalized with the extension tube wall, which is a few tens of degrees K warmer than the cell. For thermalized atoms and molecules one has:

$$\left\langle\frac{1}{v_m}\right\rangle = \sqrt{2}\left\langle\frac{1}{v_a}\right\rangle. \qquad (3)$$

Using Eqs. (1)–(3), it can be shown that the partial beam rates S_a and S_m can be combined to form the variable S_{tot} which is proportional to Φ^{TGA}

$$S_{tot} = S_a + \kappa\sqrt{2}S_m \propto \Phi^{TGA} \qquad (4)$$

where κ is the calibration constant of the TGA giving the relative sensitivity of the TGA for atomic and molecular beams

$$\kappa = \frac{\sigma_a^{ion}\,\varepsilon_a}{\sigma_m^{ion}\,\varepsilon_m}. \qquad (5)$$

Eq. (4) applies to the case of constant extension tube temperature T_{ext} and emission current I_{emiss}. Taking into account the dependence of S_a and S_m on the measured[5] T_{ext} and I_{emiss}, one can define a temperature and emission normalized nucleon flow rate ϕ_{tot} into the TGA ionizer, which is proportional to the injected ABS intensity Φ^{ABS} (neglecting the small contribution from the target chamber rest gas):

$$\phi_{tot} = \frac{S_{tot}\sqrt{T_{ext}}}{f(I_{emiss})} \propto \Phi^{ABS}. \qquad (6)$$

The quantity ϕ_{tot} is a good monitor of ABS stability over time, as it is independent of recombination inside the storage cell. Following

---

[4] The beam shutter was installed at the beginning of the deuterium running period in 1998. During the 1996/'97 hydrogen running period, the contribution of dissociative hydrogen ionization was taken into account by detecting the intensity of masses 2 and 18 amu in addition to mass 1 amu [15].

[5] A thermocouple on the extension tube was first installed at the beginning of 1999. In the 1997 analysis, the extension tube temperature was related to the cell temperature using the expression $T_{ext}(T) = T_0 + \frac{300-T_0}{300}T$, where T_0 is a constant estimated from calibration studies, and T is the measured cell temperature in K.

Eq. (6) one can also express normalized nucleon flow rates for atoms, ϕ_a, and for molecules, ϕ_m, by

$$\phi_a = \frac{S_a \sqrt{T_{ext}}}{f(I_{emiss})} \qquad (7)$$

$$\phi_m = \frac{\sqrt{2}\kappa S_m \sqrt{T_{ext}}}{f(I_{emiss})}. \qquad (8)$$

The degree of dissociation of the sample beam, defined as the fraction of nucleons in atoms relative to all nucleons entering the TGA, is given by

$$\alpha^{TGA} \equiv \frac{\phi_a}{\phi_a + \phi_m} = \frac{S_a}{S_a + \sqrt{2}\,\kappa\,S_m}. \qquad (9)$$

The degree of dissociation α^{TGA}, also called atomic fraction, is displayed by the TGA roughly once per minute.

3.2. The calibration of the TGA

The purpose of the TGA calibration is to determine the relative sensitivity κ defined by Eq. (5). The calibration can be performed by varying the relative amount of atoms and molecules at a constant injected ABS total flux:

$$\phi_{tot} = \phi_a + \phi_m = \text{const.} \qquad (10)$$

Using relations (7) and (8), one can write

$$\frac{\partial\left(\frac{S_m \sqrt{T_{ext}}}{f(I_{emiss})}\right)}{\partial\left(\frac{S_a \sqrt{T_{ext}}}{f(I_{emiss})}\right)} = -\frac{1}{\sqrt{2}\,\kappa} \qquad (11)$$

where the minus sign reflects the fact that an increase in ϕ_m must correspond to a decrease of ϕ_a. Hence a fit of the normalized molecular signal ϕ_m as function of the normalized atomic one ϕ_a results in a straight line with a slope of $-\frac{1}{\sqrt{2}\,\kappa}$.

Because the recombination process in the HERMES target is strongly temperature dependent, a controlled variation of the atomic fraction can be obtained by changing the temperature of the storage cell. A second possibility is to take advantage of an accidental beam loss in the region of the HERMES target which might temporarily change the surface property of the cell and cause a sharp drop of α^{TGA} followed by a slow recovery. The measured values for κ are reported in Table 3.

Table 3
Summary of the values of TGA calibration constant κ for the years 1997–2002

Target/year	κ
H$_\parallel$(1997)	0.551 ± 0.026
D$_\parallel$(2000)	0.861 ± 0.024
H$_\perp$(2002)	0.55 ± 0.05

A detailed description of the TGA calibration and its performance can be found in Ref. [9].

3.3. Interpretation of the BRP signals

The atomic signal detected by the BRP depends on the hyperfine population in the sample beam, the transmission probabilities of the sextupole system and on the setting of the transition units. For a stable storage cell temperature, the transmission of the magnetic system is fixed. The transition units can be switched on and off, changing the intensity of the beam reaching the detector. The BRP signal can be described by the following expression:

$$S_i = c \sum_a \left(\sum_b \sigma_b T_{ab}^i \right) I_a \qquad (12)$$

where I_a is the sample beam intensity (in atoms/s) of the atoms in hyperfine state $|a\rangle$, T_{ab}^i describes the exchange of hyperfine states by the transition unit[6] i, σ_b is the sextupole transmission probability for state $|b\rangle$, and c is a proportionality factor[7]. The goal of these measurements is to determine the four (six) sample beam intensities, I_a, for the hydrogen (deuterium) sample beam. Summing Eq. (12) over index b one obtains

$$S_i = c \sum_a M_{ia} I_a \qquad (13)$$

where the *measurement matrix* M_{ia} includes information concerning transmission probabilities and RF-transition efficiencies.

---

[6] If two units are working, the matrix T^i has to be replaced by $T_{ab}^{ij} = \sum_c T_{ac}^i T_{cb}^j$.

[7] Expression (12) simplifies into $S_{off} = c \sum_a \sigma_a I_a$ in the case that no transition unit is switched on.

Assuming that M_{ia} is known, one can solve the system of equations (13) for I_a if, during a given ABS injection status, the BRP transition units are operated in at least four (six) different modes in the case of hydrogen (deuterium). The solution is given by

$$I_a = c^{-1} \sum_i R_{ai} S_i \qquad (14)$$

where[8] $R = M^{-1}$. The total sample beam intensity, I_{tot}, is obtained by taking the sum over all hyperfine states

$$I_{\text{tot}} = \sum_a I_a. \qquad (15)$$

Finally, the relative hyperfine populations n_a are given by normalizing the intensities I_a

$$n_a = \frac{I_a}{I_{\text{tot}}}. \qquad (16)$$

The polarizations of the atoms in the sample beam can now be calculated from the target magnetic field strength, as expressed by the following vectorial forms for hydrogen and deuterium, respectively

$$(P_e, P_z)^{\text{T}} = M_{\text{P}}^{\text{H}}(n_1, n_2, n_3, n_4)^{\text{T}}$$

$$(P_e, P_z, P_{zz})^{\text{T}} = M_{\text{P}}^{\text{D}}(n_1, n_2, n_3, n_4, n_5, n_6)^{\text{T}}$$

where the matrices M_{P}^{H} and M_{P}^{D} contain the target holding field strength, e.g., for hydrogen

$$M_{\text{P}}^{\text{H}} = \begin{pmatrix} -1 & a & 1 & -a \\ 1 & -a & -1 & a \end{pmatrix} \qquad (17)$$

where a $= \frac{k}{\sqrt{1+k^2}}$, $k = B/B_c$, $B_c = 50.7\,\text{mT}$.

The statistical uncertainties of the measured signals S_i are represented by the diagonal covariance matrix C_{S}. Hence, the covariance matrix C_I of the intensities I_a is given by

$$C_I = R C_{\text{S}} R^{\text{T}} = (M^{\text{T}} C_{\text{S}}^{-1} M)^{-1}. \qquad (18)$$

The sum over all the elements of C_I gives the statistical uncertainty ΔI_{tot} of the total

intensity I_{tot}

$$(\Delta I_{\text{tot}})^2 = \sum_{ab} (C_I)_{ab}. \qquad (19)$$

The covariance matrix C_n of the hyperfine populations n_a is

$$(C_n)_{ab} = \sum_{cd} \left(\frac{\partial n_a}{\partial I_c}\right)(C_I)_{cd}\left(\frac{\partial n_b}{\partial I_d}\right) \qquad (20)$$

while the covariance matrix of the polarization vector can be calculated in the following way:

$$C_{\text{P}} = M_{\text{P}}^{\text{H,D}} C_n (M_{\text{P}}^{\text{H,D}})^{\text{T}}. \qquad (21)$$

From C_{P} one can extract the statistical uncertainty of the polarization measurement.

During normal running conditions, the entire automated procedure to measure and calculate the polarization vectors and their uncertainties took roughly 60 s (90 s) for hydrogen (deuterium), resulting in a statistical uncertainty of about ± 0.013 for hydrogen. For deuterium the statistical uncertainty was about ± 0.031 for positive and ± 0.022 for negative nuclear polarization. After an optimization of the BRP sextupole system, and an increase in the diameter of the sample tube, the statistical uncertainty of a 60 s measurement for hydrogen was reduced to less than 0.5 %.

3.4. The BRP calibration

In the previous section it was shown that the atomic polarizations can be calculated from the measured BRP signals assuming the knowledge of the measurement matrix M_{ia}. This includes the efficiencies of the transition units and the transmission probabilities of the sextupole system for various hyperfine states. The procedure used to determine these parameters is called the BRP calibration.

The basic idea of the calibration measurement is to make the system of Eqs. (13) overdetermined so that additional parameters like efficiencies or sextuple transmissions can be extracted through a fit to the data. Due to the fact that the transition units can be combined in several possible ways, the number of signals which can be collected during a polarization measurement exceeds the number of hyperfine states N_{hfs}. However, the number of

---

[8]If the number of collected signals is larger than the number of unknowns, one has to use the *pseudo-inverse* matrix $R = (M^{\text{T}} G_{\text{S}} M)^{-1} M^{\text{T}} G_{\text{S}}$, where G_{S} is the inverse covariance matrix of the measured signals. This procedure is equivalent to a fit of the intensities I_a to the signals S_i.

unknowns that can be determined in this way is still less than the total number of parameters. The problem can be overcome by cycling this measurement through several (total number N_{ABS}) injection modes (see Table 2) so that an adequate number of signals can be collected.

3.4.1. The transition efficiencies

We first discuss the method to determine the transition efficiencies, assuming a priori knowledge of the sextupole transmissions σ_n for each hyperfine state. Calibration of those transmissions will then be discussed in Section 3.4.2.

The BRP contains two transition units, a strong field (SFT) and a medium field (MFT) unit. The SFT can drive two transitions for hydrogen ($|1\rangle \leftrightarrow |4\rangle$ and $|2\rangle \leftrightarrow |4\rangle$) and five for deuterium. The efficiencies of the SFT transitions in the case of hydrogen are called ε_{s14} and ε_{s24}. The MFT is a multi-step transition unit which can drive two sub-transitions for hydrogen ($|1\rangle \leftrightarrow |2\rangle$ and $|2\rangle \leftrightarrow |3\rangle$)[9] and three for deuterium. For hydrogen the MFT is tuned either as a $|1\rangle \leftrightarrow |3\rangle$ (which is achieved by applying the $|1\rangle \leftrightarrow |2\rangle$ and $|2\rangle \leftrightarrow |3\rangle$ transitions sequentially) or as a $|2\rangle \leftrightarrow |3\rangle$ only. In the latter case the MFT unit is tuned to avoid the $|1\rangle \leftrightarrow |2\rangle$ sub-transition. Although nearly zero, the residual $|1\rangle \leftrightarrow |2\rangle$ efficiency for the $|2\rangle \leftrightarrow |3\rangle$ tune of the MFT has to be taken into account.

Due to the limited space available for the BRP equipment, there is cross-talk between the two BRP transition units when both static fields are switched on, so that the tuning of the MFT is influenced by the SFT field, whereas the SFT is not influenced by the (low) MFT field. The MFT efficiencies have to be measured separately for each SFT setting, as they depend on the exact static field. For hydrogen this leads to an increase in the number of MFT efficiencies from four to eight. The various MFT efficiencies are identified by means of the subscripts $c14$ (for SFT 1–4 static field on) or $c24$ (SFT 2–4 static field on) and by the subscripts $r13$ or $r23$ which indicate the particular sub-transition being considered. For example, the notation $\varepsilon_{m13r23c24}$ represents the efficiency of the transition MFT 1–3, step 2–3, tuned together with the static field of the SFT 2–4. The total number of efficiencies N_{eff} is 10 for hydrogen and 41 in the case of deuterium. The number N_{BRP} of possible BRP signals related to various transition states is 11 for hydrogen (as shown in Table 4) and 29 for deuterium.

If the ABS is operated in N_{ABS} different injection modes, and the BRP transition units switch through all possible N_{BRP} states, the total number of collected signals is $N_s = N_{ABS} N_{BRP}$. In this way, recalling Eq. (13), one obtains a system of N_s equations containing $N_u = N_{eff} + N_{ABS} N_{hfs}$ unknowns,[10] where $N_{hfs} = 4(6)$ in the case of hydrogen (deuterium). The system can be solved if $N_f = N_s - N_u \geqslant 0$, where N_f counts the degrees of freedom and is given by

$$N_f = N_s - N_u$$
$$= (N_{BRP} - N_{hfs}) N_{ABS} - N_{eff}. \tag{22}$$

In such a case, both the hyperfine state intensities I_a and the transition efficiencies ε can be determined. For hydrogen, the calibration measurement makes use of 7 ABS injection modes, resulting in $N_f = 39$. In the case of deuterium two possible options have been developed, one with 5 ABS modes ($N_f = 74$) and the other with 6 ($N_f = 97$).

The solution of the system is carried out by applying a Runge–Kutta method as explained in [10]. The resulting covariance matrix C_x has the form

$$C_x = \begin{pmatrix} C_\varepsilon & C_{\varepsilon,I} \\ C_{I,\varepsilon} & C_I \end{pmatrix} \tag{23}$$

where C_ε contains uncertainties and covariances of the efficiencies and is used to calculate the systematic uncertainty of the polarization measurement. The resulting systematic uncertainty induced by the determination of the transition efficiencies of the order of 1.5 %. Table 5 summarizes the transition efficiency measurements performed in 1997 with hydrogen. The efficiencies

---

[9]The order of the sub-transitions depends on the sign of the gradient field, which is negative in the HERMES BRP [15].

[10]During the evaluation of the transition efficiencies, the sextuple system transmissions probabilities are assumed to be constant.

Table 4
Possible switching modes of the BRP transition units for hydrogen running

BRP-Signal	Name	MFT-RF	MFT	SFT-RF	SFT
OFF	off	OFF	OFF	OFF	OFF
SFT 1–4	s14	OFF	OFF	ON	1–4
SFT 2–4	s24	OFF	OFF	ON	2–4
MFT 1–3	m13c14	ON	1–3	OFF	1–4
MFT 1–3	m13c24	ON	1–3	OFF	2–4
MFT 2–3	m23c14	ON	2–3	OFF	1–4
MFT 2–3	m23c24	ON	2–3	OFF	2–4
MFT 1–3/SFT 1–4	m13s14	ON	1–3	ON	1–4
MFT 1–3/SFT 2–4	m13s24	ON	1–3	ON	2–4
MFT 2–3/SFT 1–4	m23s14	ON	2–3	ON	1–4
MFT 2–3/SFT 2–4	m23s24	ON	2–3	ON	2–4

During a calibration measurement all signals are collected, while for a polarization measurement only a subset of them is chosen.

Table 5
BRP transition unit efficiencies measured during the 1997 hydrogen running fixing the sextupole transmission ratio to $r_{21} = 1.029$

Name	MFT	SFT	Efficiency (%)	Uncertainty (%)
ε_{s14}	—	1–4	99.3	1.34
ε_{s24}	—	2–4	101.0	1.03
$\varepsilon_{m13r12c14}$	1–3	1–4	101.0	1.03
$\varepsilon_{m13r23c14}$			98.6	1.41
$\varepsilon_{m23r12c14}$	2–3	1–4	−1.0	1.13
$\varepsilon_{m23r23c14}$			94.9	1.23
$\varepsilon_{m13r12c24}$	1–3	2–4	99.9	0.42
$\varepsilon_{m13r23c24}$			90.3	0.82
$\varepsilon_{m23r12c24}$	2–3	2–4	0.0	1.10
$\varepsilon_{m23r23c24}$			97.4	1.04

Each efficiency is shown along with an explanation of the MFT and SFT static field setting.

of the transitions for deuterium running can be found in Ref. [10].

3.4.2. The sextupole transmissions

In the previous section it was shown how the efficiencies ε_i of the BRP transition can be measured, assuming a priori knowledge of the sextupole transmissions σ_n for each hyperfine state. The attempt to fit both ε_i and all of the σ_n within the same algorithm fails. Nevertheless, the transmission probabilities can be determined by separating the fitting procedure into two steps, as shown below.

In the BRP (Fig. 10), atoms with $m_S = -\frac{1}{2}$ are either defocused or stopped by the beam blocker, having therefore zero transmission probability ($\sigma_3 = \sigma_4 = 0$ for hydrogen and $\sigma_4 = \sigma_5 = \sigma_6 = 0$ for deuterium). Moreover, due to the normalization (Eq. (16)), only ratios of transmission probabilities are required for measuring the hyperfine populations. Thus the remaining required parameters are σ_2/σ_1 for hydrogen and σ_2/σ_1 and σ_3/σ_1 for deuterium.

The Stern–Gerlach force of the sextupole magnets is weaker for hydrogen atoms in state $|2\rangle$ compared to state $|1\rangle$ for magnetic fields B of the order or less than the hydrogen critical field $B_c = 50.7\,\text{mT}$, near the axis of the sextupole system. Thus near-axis atoms in hyperfine states $|1\rangle$ and $|2\rangle$ will experience a different transmission efficiency and the transmission ratio $r_{12} = \sigma_1/\sigma_2$ is expected to exceed unity by a small amount. Due to the smaller hyperfine coupling of deuterium, $B_c = 11.7\,\text{mT}$, the deviation from unity of the ratio σ_2/σ_1 and σ_3/σ_4, is expected to be significantly smaller than for hydrogen. Ray tracing simulations [7] show that the deviation is in fact negligible. From these consideration it follows that the only transmission ratio that needs to be measured is $r_{21} = \sigma_2/\sigma_1$ for hydrogen.

From the BRP calibration the transition efficiencies are extracted as a function of the parameter r_{21}. The transmission ratio can thus be evaluated by minimizing the χ^2 of the calibration results. As the transmission probability of the

sextupole system depends on the velocity distribution of the atomic sample, the storage cell temperature T_{cell} has to stay constant over the calibration measurement. This procedure applied to a calibration measurement taken at $T_{cell} = 95\,K$ has produced the following result [10]:

$$\frac{\sigma_2}{\sigma_1}|_{95\,K} = 1.029 \pm 0.0015. \tag{24}$$

The small uncertainty of the measured ratio can be neglected in the calculation of the systematic uncertainty of the polarization measurement. The potential cell temperature dependence of the transition efficiencies can be neglected as the velocity distribution of the sample is fixed by the BRP sextupole system. Therefore, a polarization measurement performed collecting at least one signal more than the minimum required number (as is always the case) can be used to fit the ratio r_{21} for various cell temperatures.

A more detailed description of the BRP calibration and performance can be found in Ref. [10].

4. Processes occuring inside the storage cell

Inside the storage cell, the atoms of the target may experience several interactions that have an influence on the average target polarization P_T. Their complete understanding is therefore fundamental for the reduction of the systematic uncertainty of the target polarization. In this section an overview of these processes will be given, while a quantitative estimate of their contributions for the various running periods of the HERMES target can be found in Section 6. The processes are divided into two categories—recombination processes and spin relaxation processes.

Recombination and relaxation by wall collisions are surface effects whereas spin exchange collisions and resonant interaction of beam and target gas happen in the gas storage cell volume. The operating conditions of the target are chosen such that these unwanted effects are suppressed as much as possible. It should be noted that spin relaxation can be studied and monitored with good statistics by means of the BRP, whereas the

residual polarization after recombination can be studied only using a scattering process like deeply inelastic scattering with a much lower rate.

4.1. Recombination processes

The atoms that are injected into the HERMES storage cell may recombine to molecules, possibly keeping part of their nuclear polarization. Recombination [11] can in principle take place either on the storage cell walls (surface recombination) or in the gas phase (volume recombination). At the low gas densities of the HERMES target, volume recombination is negligible. On the cell walls two types of recombination processes with surface catalysis can be distinguished, which are expected to result in different residual nuclear polarization in the molecules:

- the Langmuir–Hinselwood (L–H) process, where two adsorbed thermalized atoms react with each other,
- the Eley–Rideal (E–R) process, where an atom from the gas phase reacts directly with an adsorbed atom [24].

The residual polarization of the surface atoms recombining through the E–R mechanism in the cell was measured with the HERMES spectrometer, making use of a well-known DIS asymmetry. The result was presented in Ref. [13] and will be discussed in Section 5.2.

Since the storage cell temperature is usually kept below 140 K, a small amount of water originating from the ABS dissociator freezes on the surface and grows into an ice layer on top of the Drifilm surface. The presence of water is important since water is known to inhibit hydrogen or deuterium recombination. Fresh storage cell coatings are hydrophobic, but secondary particles from the HERA beam quickly change the chemical structure of the Drifilm surface, causing the surface to become less hydrophobic. This was predicted to occur in the longitudinal holding field by simulations of acceleration by the beam bunch electric fields of positive ions produced by the beam in the target gas. Even when not at cyclotron resonance, the ions stochastically gain energy until they hit

the cell wall with energies of order 100 eV. Surface doses in the range 10 Gy/s can occur, depending on the magnetic holding field and the beam current. Furthermore, the downstream portion of the small cell used since December 1999 is exposed to synchrotron radiation that is single-scattered from collimator C1. Fortunately, it has been observed that during normal operation, the quality of the cell surface gradually recovers and the amount of recombination in the cell decreases, thanks to the steady accumulation of ice on the surface.

A detailed description of the recombination studies performed on the HERMES storage cell can be found in Ref. [11].

4.2. Spin relaxation

Three different atomic spin relaxation mechanisms can in principle be observed to occur in the HERMES target, as they cause a change in the hyperfine population inside the storage cell. One relaxation process takes place on the wall of the storage cell. Another is due to two-body spin-exchange collisions of atoms in the gas phase. In the third mechanism the high frequency fields generated by the passage of the very short HERA beam bunches can cause a depolarization in the target atoms under certain conditions [12]. Spin relaxation of atomic hydrogen by wall or spin exchange collisions with various types of wall coatings has been under study for many years in the context of a hydrogen maser for low holding fields [6]. For the HERMES target further studies of the magnetic field dependence of spin relaxation as well as studies of the temperature dependence and density dependence of the transition spectra have been carried out [15,25–28]. The results of these studies are summarized in the following sections.

4.2.1. Wall relaxation

The atoms injected by the atomic beam source experience several hundred wall collisions during their diffusion process through the storage cell. An attractive Van-der-Waals potential between the storage cell wall and a diffusing atom causes the atom to be physisorbed, i.e., to stay for a certain time close to the surface until it is desorbed again.

The mean residence time on the wall τ_s is described by the Arrhenius equation

$$\tau_s = \tau_0 \, e^{\left(\frac{E_b}{kT}\right)} \tag{25}$$

where τ_0 is the high temperature limit of τ_s, E_b and T are the adsorption energy and the temperature respectively, and k is the Boltzmann constant. During the time an adsorbed atom stays on the wall ($\approx 10^{-10}$ s for the HERMES cell), the magnetic moment of its unpaired electron interacts with magnetic moments on the surface by means of a dipolar coupling and/or with other unpaired electrons through exchange interactions [17–20]. Depending on the surface type, temperature and magnetic field, one can define a probability that the atom leaves the wall in a certain hyperfine state. This is described by means of transition probabilities W_{jk}, each of which represents the probability to find an atom in state $|k\rangle$ that was in state $|j\rangle$ prior to the wall collision. The theoretical description and the calculation of the transition probability matrix for the HERMES target can be found in [15].

4.2.2. Spin exchange depolarization

Atoms colliding with each other in the gas phase can undergo spin exchange, where hyperfine transitions can occur via interaction between the electron spins [29]. Due to the conservation of angular momentum, the sum of the magnetic quantum numbers m_F before and after the spin exchange collision has to be the same:

$$\Delta \sum_i m_F = 0. \tag{26}$$

One can see that if an initial population of the gas consists only of pure state $|1\rangle$ or $|3\rangle$ in the case of hydrogen and $|1\rangle$ or $|4\rangle$ in the case of deuterium, no relaxation by means of spin exchange is possible. This is actually not the case for the HERMES cell, where to double the density, more than one atomic state is injected during normal operation. The effect of spin exchange collisions on the hyperfine populations can be described by a tensor M_{jk}^i, which gives the probability to find an atom in state $|i\rangle$ after a collision of two atoms in the state $|j\rangle$ and $|k\rangle$ prior to the collision: The number of spin exchange collisions per unit time

and volume is

$$\dot{N}_{se} = n^2 \sigma_{se} \langle v_r \rangle \tag{27}$$

where n is the gas density, σ_{se} is the spin-exchange cross-section and v_r is the relative velocity of the atoms. The density dependence of spin-exchange collision relaxation, combined with the knowledge of σ_{se} [30,31], was used to determine the density inside the HERMES cell [15]. The results will be reported in Section 6.

4.2.3. Evolution equation for the description of the spin relaxation process

The various spin relaxations due to wall collisions and spin exchange collisions cannot be treated separately. After an interaction with the surface during a wall collision, an atom in the gaseous phase can then interact through spin exchange collision and, at the next wall collision, interact again with the surface. Since the atoms are constantly exposed to both interactions, an appropriate description is given by an evolution equation for the hypefine fractional populations n_i of the hyperfine state $|i\rangle$ [15,25][11]:

$$\frac{dn_i}{dt} = \frac{1}{\tau_d}(n_i^{inj} - n_i) + \frac{1}{\tau_f} \sum_k R_{jk} n_k$$
$$+ \frac{1}{\tau_{se}} \sum_{jk} M_{jk}^i n_j n_k. \tag{28}$$

The first two terms of Eq. (28) characterize the incoming and outgoing fluxes, the third term represents the wall relaxation and the last term the spin exchange relaxation. The effect of recombination is not included, and it is assumed that the total flux from the ABS is constant with time. In Eq. (28), three time constants appear: τ_d (the diffusion time) is the mean occupation time of atoms within the storage cell, τ_f is the mean time of flight between two wall collisions and τ_{se} is the mean time of flight between two spin exchange collisions. For times that are large compared to τ_d, the relative hyperfine populations converge toward a dynamic equilibrium (*steady state*). As an example of the application of Eq. (28), the solution

---

[11]In these references, this equation is designated as the *master equation*.

of the system of linear equations in the steady state (with $\frac{dn_i}{dt} = 0$) was solved directly in the case of hydrogen or with the help of a numerical iteration algorithm in the case of deuterium [15]. Fig. 11 represents the measured hyperfine fractional populations as a function of the magnetic field for hydrogen and a fit to the data using the solutions of Eq. (28). The fitted parameters are the three time constants and optionally the injected atomic state fractional populations. The R and M transition probability matrices are calculated on the basis of theoretical models [15]. These data show that a holding field greater than 300 mT is needed to have sizable polarization for the case of two injected states.

4.2.4. Bunch field induced depolarization

The beam of the HERA electron storage ring is bunched with time period $\tau_{bunch} = 96.1$ ns between two adjacent bunches. Typically, most of the 220 RF buckets are filled, so that the bunch frequency is given by:

$$v_{bunch} = \frac{1}{\tau_{bunch}} = 10.42 \, \text{MHz}. \tag{29}$$

A large number of harmonics contribute to the induced magnetic high-frequency field close to the HERA beam, because the bunches are very short ($\sigma = 30$ ps). The transition frequency between two hyperfine states $|i\rangle$ and $|j\rangle$ is given by:

$$v_{ij} = \frac{E_i(B) - E_j(B)}{h}. \tag{30}$$

If v_{ij} matches one of these harmonics at a certain holding field B, resonant depolarization occurs. The location of the beam-induced resonances is shown in Fig. 12. Bunch field induced depolarization at the HERMES target has been studied in the cases of hydrogen [12,28] and deuterium [15] for the longitudinal orientation of the target holding field (before 2001). During this time the observed π ($\Delta m = \pm 1$) transitions were sufficiently well separated so that at the working field (335 mT) no beam induced depolarization could be found. In the case of the transverse field that has been in use since October 2001, both σ ($\Delta m = 0$) and π ($\Delta m = \pm 1$) transitions are allowed because the oscillating field surrounding the
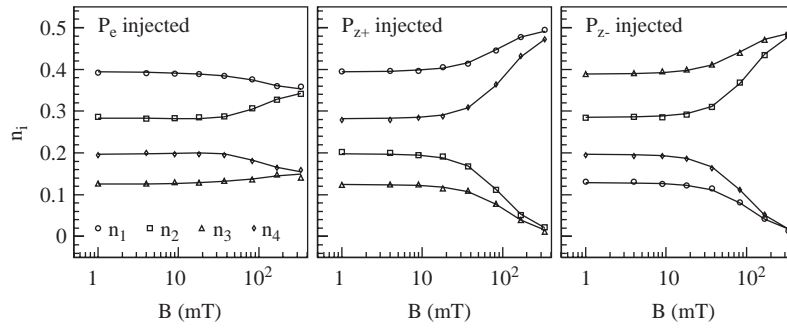
Fig. 11. Measured fractional hyperfine populations vs. magnetic field for hydrogen for the various injection modes. The measured values are given by symbols, while the lines show a fit using the solutions of Eq. (28).
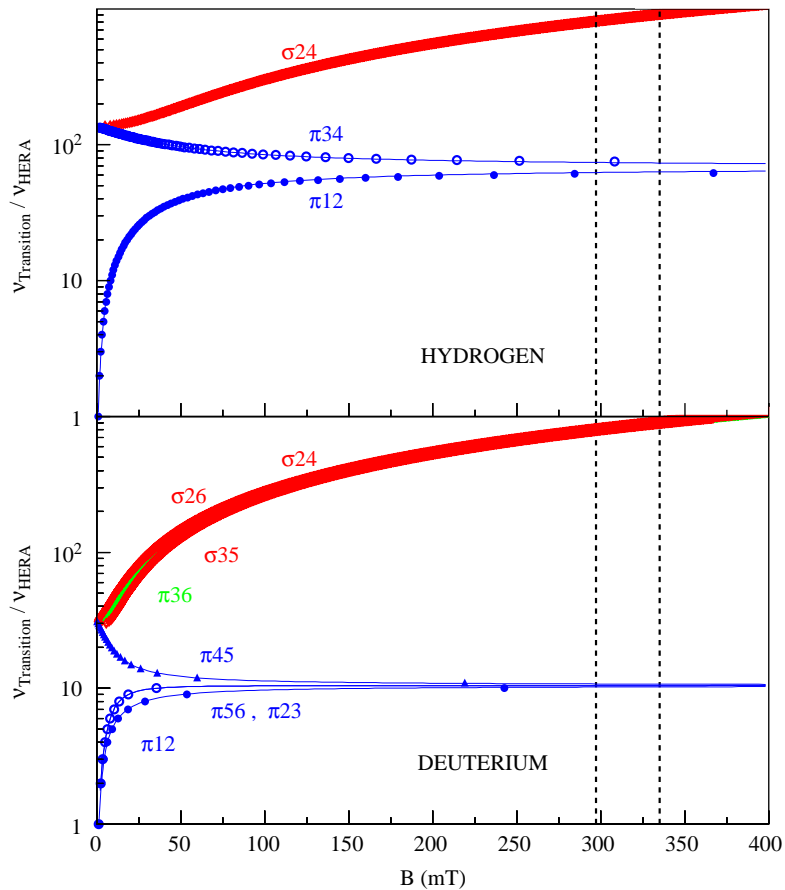

Fig. 12. Possible beam-induced nuclear depolarizing resonances in the HERMES target. The frequency difference between pairs of hyperfine states whose transitions lead to nuclear depolarization are plotted as a function of the holding field. The frequency values are normalized to $\nu_{HERA} = 10.42$ MHz. The symbols representing the resonance conditions are clearly distinguishable for the π transitions, while they overlap with each other in the case of σ and $\pi|3\rangle \leftrightarrow |6\rangle$ transitions, which are separated by a difference in the intensity of the holding field ΔB_T of only 0.37 mT. The dashed lines represent the working fields of the transversely (left) and longitudinally (right) polarized targets.

HERA beam has components both parallel and perpendicular to the static holding field. The spacing between two adjacent resonances is narrower than in the longitudinal case (only 0.37 mT difference in the magnetic holding field at $B = 0.3$ T), so a better homogeneity in the holding field is needed (see Fig. 12).

Thus a transverse field value for which beam resonant depolarization can be completely suppressed does not exist. A pair of additional correction coils mounted closely around the storage cell to improve the field homogeneity was installed for the 2003 running to further reduce resonant depolarization. The results will be presented in a forthcoming paper.

5. Target polarization

The average polarization P_T of the nucleons in the target is a fundamental parameter of the HERMES experiment. The problem is to relate the measured atomic polarizations in the sample beam with the density-weighted average polarization of the nuclei in the cell. The determination of the target polarization involves several terms that mainly account for two effects:

- Presence of molecules in the cell, both unpolarized from the residual gas of the scattering chamber and/or directly injected from the ABS, and polarized molelcules coming from recombination of polarized atoms on the cell surface.
- Relaxation and recombination effects in the storage cell leading to an inhomogeneous distribution of the atomic fraction and of the atomic polarization.

The average target polarization P_T as seen by the electron beam is given by the following equation:

$$P_T = \alpha_0 \alpha_r P_a + \alpha_0 (1 - \alpha_r) \beta P_a \qquad (31)$$

where α_0 represents the initial fraction of nucleons in atoms in the gas injected by the ABS (or atomic fraction in the absence of recombination), α_r denotes the fraction of nucleons in atoms that have survived recombination, and $\beta = P_m/P_a$

represents the ratio of the nuclear polarization of the molecules P_m produced by recombination relative to the nuclear polarization of the atoms P_a. The knowledge of β for the experimental conditions at the HERMES experiment will be discussed in Section 5.2.

The values for α_0, α_r and P_a are calculated using the measurements of the TGA and BRP combined with various calibrations. As both detectors measure the properties of a sample of the target gas from the center of the target cell, it is necessary to relate the results to a corresponding value averaged along the storage cell. This is achieved by evaluating the sampling corrections [14]:

$$c_\alpha \equiv \frac{\alpha_r}{\alpha_r^{TGA}} \qquad (32)$$

$$c_P \equiv \frac{P_a}{P_a^{BRP}}. \qquad (33)$$

The sampling corrections and their systematic uncertainties are functions of the measured values of α_r^{TGA} and P_a^{BRP}, respectively. The functions depend on the geometry of the storage cell, its surface properties and the detectors' acceptances. They are calculated with the help of Monte Carlo simulations of the stochastic motion of particles in the storage cell, where the histories of these particles are stored and analyzed. Another possibility is to calculate sampling corrections analytically by describing the diffusion process of the target gas inside the storage cell with the use of a one-dimensional diffusion equation. The issue was addressed in Ref. [14] and will be discussed here in Section 5.4.

The various quantities entering the calculation of the average polarization are summarized in Table 6.

5.1. Determination of the quantities α_r and α_0

In order to calculate the target polarization following Eq. (31), it is necessary to separate the atomic fraction α_0 that would be seen by the HERA electron beam if no cell wall recombination were to occur and the fraction α_r of the initially injected atoms that survive wall recombination, as seen by the HERA electron beam. The measured

Table 6
Meaning of the quantities contained in Eq. (31)

Quantity	Meaning
P_T	Density-averaged nuclear polarization in the cell
α_0	Atomic fraction in the absence of recombination within the cell
$\alpha_r = c_\alpha \alpha_r^{TGA}$	Fraction of atoms surviving recombination in the cell
c_α	Sampling correction for the atomic fraction
α_r^{TGA}	Measured atomic fraction in the sample beam
$P_a = c_P P_a^{BRP}$	Nuclear polarization of atoms in the cell
c_P	Sampling correction for the atomic polarizations
P_a^{BRP}	Measured nuclear polarization of atoms in the sample beam
$\beta = P_m / P_a$	Relative nuclear polarization of recombined atoms

quantity α^{TGA} can also be factored in two terms and can be written as (see Eq. (9)):

$$\alpha^{TGA} = \frac{\phi_a}{\phi_a + \phi_m} = \alpha_0^{TGA} \alpha_r^{TGA}. \qquad (34)$$

Since dissociative ionization can be neglected [7], the only source of atomic flux ϕ_a into the gas analyzer is that originating from the atomic beam source. The molecular flux ϕ_m may come from three different sources:

- Undissociated molecules ballistically injected by the ABS. Since the efficiency of the dissociator is around 80%, a significant number of molecules pass through the nozzle towards the polarizing stage, affected by neither the sextupole magnets nor the transition units. Although the majority of these molecules hits the vacuum chamber wall and is pumped away, a small number enters the storage cell via the injection tube. These unpolarized molecules have a triangular density distribution along the cell axis, with the maximum density at the center of the cell.
- Rest gas in the target chamber. These molecules originate mainly from the recombination of atoms that have left the storage cell and have thermalized on the vacuum chamber walls. This molecular component is clearly unpolarized and results in a uniform density component inside the storage cell.
- Atoms that recombine into molecules while in the cell. As explained in Section 2.3, the cell material and temperature are optimized in order to limit the depolarization and recombination effects in the target atomic gas. Nevertheless, atoms can stick on the cell surface and recombine, and the resulting molecules may carry a residual nuclear polarization.

The normalized total molecular flow rate ϕ_m of atoms into the TGA ionizer can be decomposed in the following way:

$$\phi_m = \phi_{bal} + \phi_{rg} + \phi_r \qquad (35)$$

where ϕ_{bal}, ϕ_{rg} and ϕ_r represent the ballistic, the rest gas and the recombination components, respectively. To separate between polarized and unpolarized molecules, we rewrite the two factors in Eq. (34) using the three contributions appearing in Eq. (35)

$$\alpha_r^{TGA} \equiv \frac{\phi_a}{\phi_a + \phi_r} \qquad (36)$$

$$\alpha_0^{TGA} \equiv \frac{\phi_a + \phi_r}{\phi_a + \phi_r + \phi_{bal} + \phi_{rg}}. \qquad (37)$$

The independent measurement of each of the three components of the total molecular flow rate is accomplished by means of routine *target calibrations*, which are usually performed between two HERA electron fills when the HERMES spectrometer is not taking data. The rest gas contribution ϕ_{rg} to the molecular flux is linearly proportional to the pressure in the target chamber. The constant of proportionality is determined by injecting into the target chamber increasing quantities of hydrogen (deuterium) molecules with a controlled flow system and by measuring the corresponding TGA count rates. The ballistic flux contribution ϕ_{bal} can be measured by varying the atomic flux of the injected beam while keeping the molecular flux constant. The atomic flux is changed by using the hyperfine transitions to select either 1 or 2 (or 3 in the case of deuterium) hyperfine states. Since the recombination

probability inside the cell was found to be independent of the injected beam intensity [10], the quantity ϕ_{bal} can be extracted. Eq. (35) is then solved for the remaining molecular flux ϕ_r. After the molecular contributions ϕ_{rg}, ϕ_{bal} and ϕ_r are extracted, one can determine α_r^{TGA} using Eq. (36) and thus α_r using Eq. (32) with the sampling correction c_α determined as described in Section 5.4. A detailed description of how these calibrations are performed was given in Ref. [8].

The factor α_0 is defined in terms of the nucleon thicknesses $t_{a,r,bal,rg}$ in the cell seen by the HERA beam

$$\alpha_0 \equiv \frac{t_a + t_r}{t_a + t_r + t_{bal} + t_{rg}}. \tag{38}$$

It can be determined without reference to additional sampling corrections. All the ϕ_i terms in Eq. (37) represent nucleon fluxes. Let us define a proportionality constant c representing the TGA response to atoms through the relationship $\phi_a = ct_a$. The fluxes ϕ_r, ϕ_{bal} and ϕ_{rg} are suppressed by a factor of $\sqrt{2}$ due to the smaller molecular velocity, leading to $\phi_r = ct_r/\sqrt{2}$ and $\phi_{bal} = ct_{bal}/\sqrt{2}$. Furthermore, in the limiting case of small cell wall recombination, the densities of atoms and molecules producing t_a, t_{bal} and t_r are triangular. In contrast, the rest gas producing t_{rg} has a uniform density along the cell, resulting in $\phi_{rg} = ct_{rg}/(2\sqrt{2})$. If the difference between the conductances of the atoms and molecules is neglected so that they have the same distributions along the cell, the above considerations can be combined to give

$$\alpha_0 = \frac{\phi_a + \sqrt{2}\phi_r}{\phi_a + \sqrt{2}(\phi_r + \phi_{bal} + 2\phi_{rg})}. \tag{39}$$

However, this difference in conductances can be taken into account [15,23], leading to different distributions along the cell and a more complicated expression

$$\alpha_0 = \frac{d(\phi_a + \phi_r)}{d(\phi_a + \phi_r) + \sqrt{2}(\phi_{bal} + 2\phi_{rg})} \tag{40}$$

where $d = \sqrt{2}/(1 + (\sqrt{2} - 1)\alpha_r)$.

5.2. Relative polarization β of nuclei in recombined atoms

As mentioned in the previous sections, some of the polarized hydrogen or deuterium atoms may recombine in the storage cell. A direct measurement of the remnant polarization contained in the molecules is not possible at HERMES, as the Breit–Rabi polarimeter can measure the atomic polarizations only. Atomic recombination is a surface-mediated temperature-dependent process [11,15]. Hence measurements of the nuclear polarization of recombined atoms using storage cells of various materials and/or with various coatings [32,33] are not directly applicable to the HERMES case. Without any information about the polarization β of nucleons in molecules (or molecular polarization in short) one has to allow in Eq. (31) the conservative range $0 \leqslant \beta \leqslant 1$. A set of data taken in 1997 at a higher cell temperature (260 K instead of the nominal 100 K) was used to measure β for hydrogen at that temperature, resulting in $\beta^{260\,K} = 0.68 \pm 0.09_{stat} \pm 0.06_{syst}$ [13]. This result can be used as an upper limit for β at 100 K ($\beta_{high}^{100\,K}$) under the following assumptions. The main mechanism responsible for recombination at 100 and 260 K is the same (i.e., the E–R mechanism) [11]. At 100 K, the recombination probability is smaller than at 260 K, because the atoms impinging from the volume have less kinetic energy to overcome the activation barrier. The residence time of chemically adsorbed atoms on the surface at 100 K is greater than at 260 K, and their possible polarization cannot exceed the value measured at 260 K. This results in $\beta_{high}^{100\,K} = 0.83$.

The lower limit for $\beta^{100\,K}$ ($\beta_{low}^{100\,K}$) can be derived from a simple argument. By assuming that the nucleon spins are not affected by the recombination process, the nuclear polarization of the molecule at the time of its formation (P_m^0) can be evaluated by taking the average value of the polarization of an atom coming from the volume (P_a) and one resident on the surface (P_s). The theoretical lower limit for $\beta^{100\,K}$ can then be inferred by supposing that atoms sticking on the cell surface are totally depolarized ($P_s^{100\,K,low} = 0$)

and applying the equation

$$\beta_{\text{low}}^{100\,\text{K}} = \frac{P_{\text{m}}^{100\,\text{K,low}}}{P_{\text{a}}^{100\,\text{K}}}$$

$$= \frac{P_{\text{a}}^{100\,\text{K}} + P_{\text{s}}^{100\,\text{K,low}}}{2} \frac{1}{P_{\text{a}}^{100\,\text{K}}}. \tag{41}$$

The result is $\beta_{\text{low}}^{100\,\text{K}} = 0.5$. A factor of 0.9 takes into account the depolarization of molecules while colliding with the walls [12,33], ending in $\beta_{\text{low}}^{100\,\text{K}} = 0.45$. Hence, the range of $\beta^{100\,\text{K}}$ can be limited to

$$0.45 \leqslant \beta^{100\,\text{K}} \leqslant 0.83. \tag{42}$$

The corresponding value and uncertainty of $\beta^{100\,\text{K}}$ are therefore given by

$$\beta^{100\,\text{K}} = 0.64 \pm 0.19. \tag{43}$$

5.3. Injected atomic polarizations

An important parameter for the evaluation of the target polarization is the injected atomic polarization $P_{\text{a}}^{\text{inj}}$ (i.e., the nuclear polarization of atoms in the absence of depolarization), as it enables the separation of the various spin-relaxation effects. The injected polarization for each ABS operating mode (Table 2) can be calculated if the transmission probabilities of the sextupole system and the efficiencies of the adiabatic transition units are known. The sextupole transmission probabilities for hydrogen and deuterium have been calculated using a Monte Carlo simulation and the results are given in Ref. [7]. The injected polarization is fairly insensitive to these values. The efficiencies of the transitions of the ABS can be extracted by measuring the magnetic field dependence of the spin relaxation processes and by fitting the data with a theoretical model described in Section 4.2.3 and given by Eq. (28). For normal operation, the important ABS injection modes are those having a large positive or negative nuclear polarization, P_{z+} and P_{z-} respectively, and, in the case of deuterium, the two additional positive and negative tensor polarization (P_{zz+} and P_{zz-}) modes (see Table 2).

For hydrogen, only two transitions after the sextupole system are used: the SFT 2–4 for P_{z+} and WFT 1–3 for P_{z-}. Therefore, the injected

polarizations are directly given by the transition efficiencies whose values have been extracted in Ref. [15] with the technique mentioned above, and cross-checked using a more direct method based on the symmetry of the spin relaxation processes for the two injection modes. In the case of deuterium, several transition units are used to provide the four polarizations, some of which are located between the two sextupole subsystems. Hence, the injected polarizations have to be calculated taking into account the transition efficiencies as well as the transmission probabilities for atoms whose hyperfine state gets changed between the two subsystems.

The calculated polarization for the hydrogen and deuterium beams injected into the target are summarized in Table 7. The degree of nuclear polarization injected by the ABS when running with deuterium is substantially lower than for hydrogen. The reason is that, due to the higher number of hyperfine states, the deuterium nuclear polarization can be achieved only by using the transition units located between the two magnetic subsystems, resulting in an incomplete separation of states.

5.4. Sampling corrections

The sampling correction functions $c_\alpha(\alpha_{\text{r}}^{\text{TGA}})$ and $c_{\text{P}}(P_{\text{a}}^{\text{BRP}})$ depend strongly on the distribution of recombination and wall relaxation probabilities per wall collision along the storage cell. For a freshly produced storage cell that has not yet been

Table 7
Estimated polarizations for the hydrogen and deuterium atomic beams injected by the ABS into the target

Mode	Hydrogen	Deuterium
P_{z+}^{inj}	97.26 ± 0.05	87.78 ± 0.07
P_{z-}^{inj}	-97.38 ± 0.07	-89.50 ± 0.10
P_{zz+}^{inj}	—	96.22 ± 0.38
P_{zz-}^{inj}	—	-177.30 ± 0.61

All values are multiplied by 100. The quoted uncertainties take only the dominant uncertainties of the ABS efficiencies into account. The values refer to the polarization of injected gas with the 0.3 T holding field. Note that, due to the standard way of defining it, the maximum achievable negative tensor polarization is -200.

exposed to the HERA beam, one can assume that the recombination and wall relaxation probabilities are constant over the entire surface of the storage cell, or at least that microscopic inhomogeneities due to various types of surface sites are equally distributed. Possible mechanisms by which the HERA beam could affect the surface properties of the storage cell include:

- desorption of the surface coating by synchrotron radiation,
- bombardment of the storage cell walls with charged particles leading to radiation damage,
- chemical reactions of ionized hydrogen or deuterium radicals with the cell surface,
- redistribution of the ice layer on the storage cell by RF heating due to the wake fields,
- contamination of the storage cell surface by sputtered material from the collimator upstream of the target.

Under normal operating conditions no influence of the HERA beam on the target performance has been observed. Nevertheless certain distinct incidents affecting the cell have been observed, when the beam tune was not optimal or the HERA beam was accidentally lost near the HERMES target region. Since the effect of the HERA beam on the surface properties is poorly known, every realistic distribution of recombination and wall relaxation probabilities has to be considered when evaluating the sampling corrections. It is therefore convenient to distinguish certain scenarios of special interest.

- Homogeneous cell (HC): the natural assumption for a freshly produced cell not yet exposed to the HERA beam. The calculated sampling corrections set an upper limit for α_r and P_a for any given values of α_r^{TGA} and P_a^{BRP}, respectively.
- Homogeneous beam tube (HBT): the main cell tube is homogeneously affected by the beam, while the side tubes are unaffected.
- Inhomogeneous beam tube (IBT): The main cell tube is inhomogeneously affected by the beam, while the side tubes are unchanged. This scenario does not lead to a single sampling correction, but it can be used to calculate a lower limit for α_r or P_a for any given value of α_r^{TGA} or P_a^{BRP}, respectively.

A model for calculating the sampling corrections was developed in Ref. [15]. It is based on a parameter $\gamma_r(\gamma_d)$, the recombination (spin-flip) probability during a wall collision. If these probabilities were constant and equal for the beam and sample tubes, the sampling corrections would depend only on their geometry. This is actually the case for a freshly installed cell, whose Drifilm coating is known to be intact and uniform. In all scenarios it is assumed that the relation $\gamma_r^{ST} \leqslant \gamma_r^{BT}$ holds at any time for the recombination probabilities in the sample tube, γ_r^{ST}, and beam tube, γ_r^{BT}. The validity of this hypothesis is proven by the data [15,23]. The numerical calculations of the sampling corrections have been performed using a molecular flow simulation, complemented by analytic calculations based on the one-dimensional diffusion equation [15].

The sampling correction c_P must be subdivided into two terms, one for the wall collisions and a second term for spin exchange relaxation, as the two processes must be treated in different ways. This can be done by defining the depolarization factors D_{wd} (wall collisions) and D_{se} (spin exchange relaxation) so that for small spin relaxation, one has

$$c_P \equiv \frac{P_a}{P_a^{BRP}} \simeq \frac{D_{wd} D_{se} P_a^{inj}}{D_{wd}^{BRP} D_{se}^{BRP} P_a^{inj}}. \qquad (44)$$

As the spin exchange relaxation occurs in the gas phase, and for the typical values of $\alpha_r > 0.9$ the atomic density distribution is little affected by any change of the cell surface properties, the relation between D_{se} and D_{se}^{BRP} is similar for all of the listed scenarios. Moreover, since calculations have shown that $D_{se} \simeq D_{se}^{BRP}$ [15], one can conclude that the sampling correction c_P is determined by the wall depolarization only

$$c_P = \frac{P_a}{P_a^{BRP}} \simeq \frac{D_{wd}}{D_{wd}^{BRP}}. \qquad (45)$$

As an example, in Fig. 13 the effect of the calculated sampling corrections for the large-aperture cell used in the 1996–97 running with hydrogen is shown. During normal operation, the values of α_r^{TGA} and D_{wd}^{BRP} are found to be almost
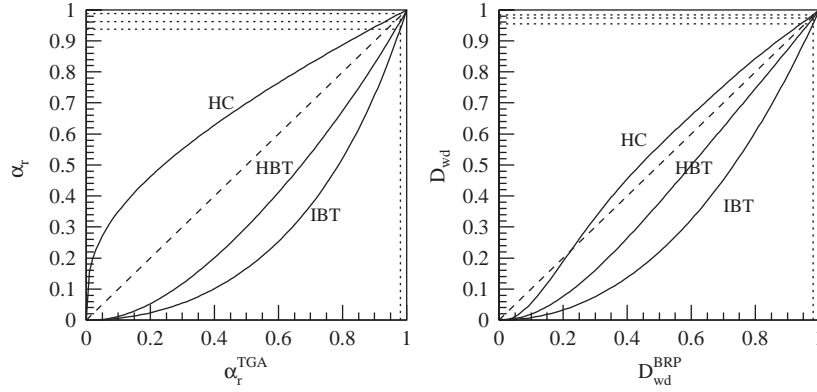
Fig. 13. Simulated correlation between the values measured by the TGA or BRP detectors and their corresponding density-weighted average values in the storage cell. The three solid curves represent the three scenarios for the state of the cell surface: homogeneous cell (HC), homogeneous beam tube (HBT), and inhomogeneous beam tube (IBT). The left figure shows the range for recombination and the right picture shows the range for wall depolarization. Acceptable uncertainties of α_r and D_{WD} (differences among the three horizontal dotted lines) can be achieved only with α_r^{TGA} and D_{WD}^{BRP} close to unity (vertical dotted lines). The corresponding uncertainty grows rapidly with increasing recombination or depolarization.

always well above 0.9, so that local linear approximations may be fitted to the calculated sampling corrections:

$$\alpha_r = \bar{a} + (1 - \bar{a})\,\alpha_r^{TGA} \tag{46}$$

$$= \alpha_r^{TGA} + \bar{a}(1 - \alpha_r^{TGA}) \tag{47}$$

$$D_{wd} = \bar{b} + (1 - \bar{b})\,D_{wd}^{BRP} \tag{48}$$

$$= D_{wd}^{BRP} + \bar{b}(1 - D_{wd}^{BRP}). \tag{49}$$

The values of the parameters $\bar{a}$ for recombination and $\bar{b}$ for depolarization are fitted to the average between the two extreme scenarios shown in Fig. 13, and their systematic uncertainties $\Delta\bar{a}$ and $\Delta\bar{b}$ are taken to be the differences found when fitting the extremes.

5.5. Evaluation of the systematic uncertainty in P_T

After having determined all the terms of Eq. (31), P_T can be expressed as a function of the measured quantities. It is convenient to write the target polarization in the following way:

$$P_T = \alpha_0(\alpha_r + (1 - \alpha_r)\beta)P_a = \alpha_{eff} \cdot P_a \tag{50}$$

where the term α_{eff} is called *effective* atomic fraction.

5.5.1. Uncertainty of the effective atomic fraction α_{eff}

Combining Eqs. (50), (47), (40), (36) and (35), α_{eff} can be expressed as

$$\alpha_{eff} = \frac{\phi_a + (\bar{a}(1 - \beta) + \beta)(\phi_m - \phi_{bal} - \phi_{rg})}{\phi_a + \phi_m + (\sqrt{2} - 1)\phi_{bal} + (2\sqrt{2} - 1)\phi_{rg}}. \tag{51}$$

The systematic uncertainty of α_{eff} is determined by the measured flow rates ϕ_a, ϕ_m, ϕ_{bal} and ϕ_{rg} and their uncertainties as well as the values and uncertainties of β, $\bar{a}$ and the TGA calibration constant κ. With the matrix T defined by

$$T = \left(\frac{\partial \alpha_{eff}}{\partial \phi_i}, \ldots, \frac{\partial \alpha_{eff}}{\partial \kappa}\right) \tag{52}$$

and the diagonal covariance matrix C of all calibration constants, the systematic uncertainty in α_{eff} is given by

$$\Delta_{sys}\alpha_{eff} = \sqrt{TCT^T}. \tag{53}$$

The matrix T contains 10 independent derivatives, i.e., for κ, $\bar{a}$, β and the seven additional terms related to the ballistic flux and rest gas calibrations as described in Ref. [9].

5.5.2. Uncertainty of the atomic polarizations P_a

Combining Eqs. (44), (45) and (49), the average nuclear polarization P_a of atoms in the HERA beam can be written as

$$P_a = P_a^{\mathrm{BRP}} + \bar{b}(D_{\mathrm{se}} P_a^{\mathrm{inj}} - P_a^{\mathrm{BRP}}). \qquad (54)$$

For the calculation of the systematic uncertainty $\Delta_{\mathrm{sys}} P_a$, the important uncertainty sources to be included are $\Delta \bar{b}$ and $\Delta_{\mathrm{sys}} P_a^{\mathrm{BRP}}$.[12] As a result, one finds

$$\Delta_{\mathrm{sys}} P_a = ((1 - \bar{b})^2 (\Delta_{\mathrm{sys}} P_a^{\mathrm{BRP}})^2$$
$$+ (1 - D_{\mathrm{wd}})^2 D_{\mathrm{se}}^2 (P_a^{\mathrm{inj}})^2 \Delta \bar{b}^2)^{1/2}. \qquad (55)$$

During the analysis one typically averages over a large dataset, so that the statistical uncertainty of the polarization measurement $\Delta_{\mathrm{sta}} P_a$ is negligible.

6. Performance

In the present section an overview is given about the target performance in the running period 1996–2003, by analyzing distinct periods for each target:

- 1997 for the longitudinal hydrogen target,
- 2000 for the longitudinal deuterium target,
- 2002 for the transverse hydrogen target.

6.1. Longitudinal hydrogen running in 1997

The upper plot in Fig. 14 shows the atomic fraction α^{TGA} measured by the target gas analyzer during the 1997 running period. The nuclear polarization of atoms measured by the BRP is plotted in the lower half of Fig. 14. Aside from startup problems, the target performance was relatively smooth. Unfortunately, a severe HERA beam loss close to the HERMES region occurred at a certain point (left line), resulting in a change of the cell surface properties. After this bad event, it was decided to collect a set of data at higher temperature ($T_{\mathrm{cell}} = 260\,\mathrm{K}$ instead of the nominal value $T_{\mathrm{cell}} = 100\,\mathrm{K}$) in order to measure the β

---

[12]The uncertainties on ΔP_{se} and on P_a^{inj} are negligible.

parameter (see Ref. [13]). At the end of this period, the storage cell was exchanged (middle line). Also the second cell experienced a beam loss (right line) which produced a small hole in the cell wall. For these reasons, the analysis of the 1997 dataset was divided into four periods, during each of which the cell surface condition was assumed to be constant. For each period, specific studies have been performed to limit the uncertainties on α_r and P_a [23].

For the entire running period with hydrogen, we quote a luminosity-weighted average value for the target polarization of $P_{z+} = -P_{z-} = 0.852 \pm 0.033$ and a density of 7.6×10^{13} nucl./cm^2 The latter number was derived from a method exploiting the density dependence of spin exchange collisions [15].

6.2. Longitudinal deuterium running in 2000

Over the eight month period of deuterium running in 2000, the HERMES target operated under very stable conditions. The atomic beam source, equipped with a microwave dissociator, experienced only one major failure, which hardly affected data accumulation. Neither the scattering chamber nor the TGA/BRP vacuum system had to be opened, leading to constant amounts of residual gas in the storage cell as well as stable efficiencies of the detectors monitoring the target. There was no need to replace the storage cell, as its performance in terms of atomic recombination and nuclear depolarization was always excellent. The reason for such good behavior can be found both in a particularly fortunate Drifilm coating and in the limited damage caused by a very well tuned electron beam, i.e., no unwanted beam losses in the vicinity of the target.

The outstanding performance of the HERMES target in this period is well represented in Fig. 15 (note the change in scale compared to Fig. 14). The stable behavior of the cell surface in terms of atomic recombination is demonstrated in the upper plot of Fig. 15, where the atomic fraction measured by the target gas analyzer is plotted. The lower plot shows the nuclear polarization. In the period between January and June 2000, the target was operated with only positive and negative states
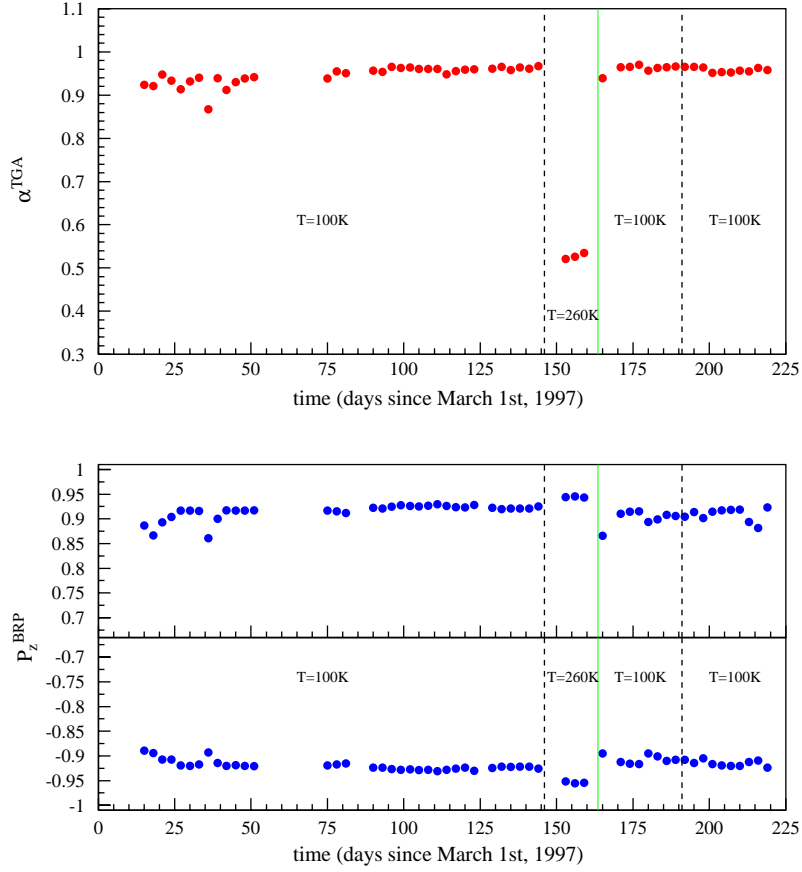
Fig. 14. The TGA (above) and BRP (below) measurements for the entire 1997 data taking period. The vertical dashed lines indicate HERA beam loss events which affected the cell surface properties, and the solid line indicates the replacement of the target cell.

of nuclear vector polarization, implying positive tensor polarization. From July on, a new injection mode combining vector and tensor polarization P_{z+}, P_{z-}, P_{zz+} and P_{zz-} was established in order to perform the first measurement of the tensor-polarized structure function b_1^d.

The average values for the four polarization states used in 2000 are the following:

$$P_{z+} = +0.851 \pm 0.029 \tag{56}$$

$$P_{z-} = -0.840 \pm 0.026 \tag{57}$$

$$P_{zz+} = +0.891 \pm 0.027 \tag{58}$$

$$P_{zz-} = -1.656 \pm 0.049. \tag{59}$$

Note that only the systematic uncertainty is quoted as the statistical uncertainty is negligible in comparison. The differences between the systematic uncertainties originate from the injection mode dependent systematic uncertainty of the atomic polarizations. The measured target density for this period, measured by means of the spin-exchange collision relaxation method, is 2.1×10^{14} nucl./cm^2.

6.2.1. Spin relaxation

The spin-flip probability per wall collision γ_d is proportional to τ_s, the mean residence time: $\tau_s = \tau_0\, e^{\left(\frac{E_b}{kT}\right)}$ (see Eq. (25)). Therefore γ_d depends on the wall temperature T. In other words, if P_a^{BRP} does not change with T, wall depolarization effects are vanishingly small within the experimental
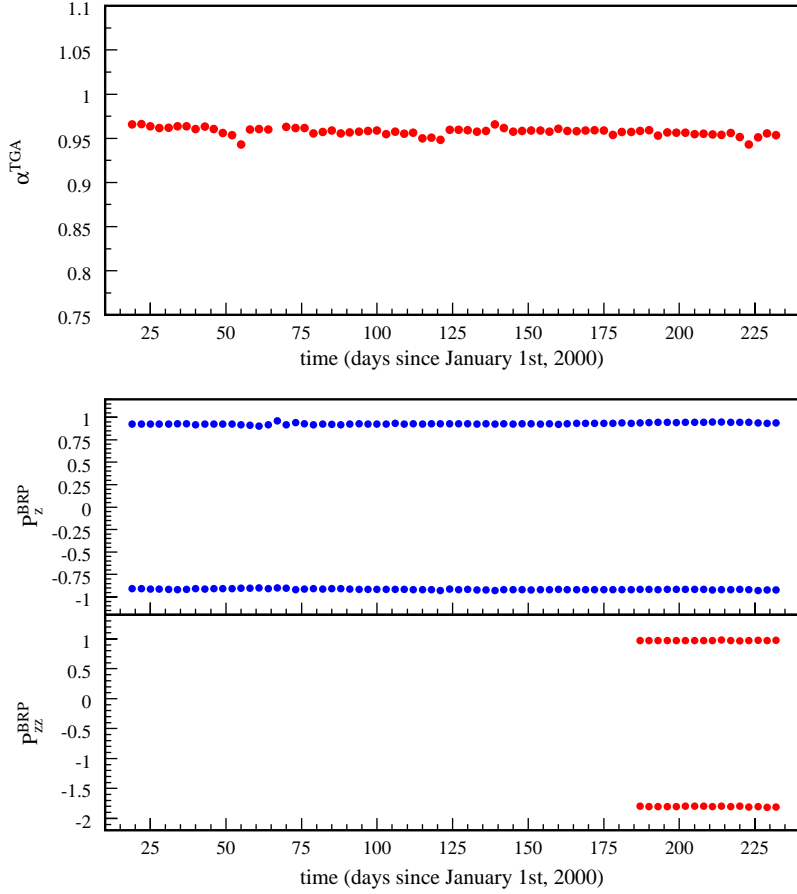
Fig. 15. Atomic fraction, α^{TGA} upper plot, and vector/tensor polarization, P^{BRP} lower plots, measured by TGA and BRP respectively during the year 2000 running period. Each symbol represents data averaged over a 72-h bin. The absolute bin averaged values are always above 0.9. The tensor polarization (lower plot) was employed from July on.
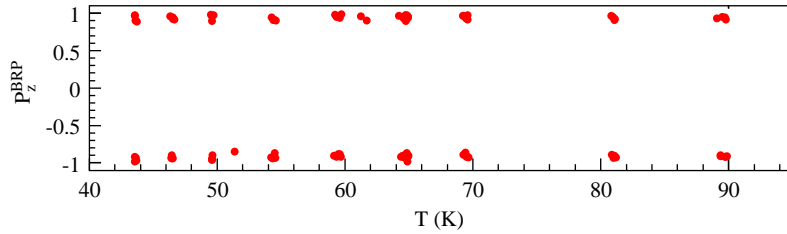

Fig. 16. Nuclear vector polarization P_z^{BRP} as function of the cell temperature T measured in August 2000. No dependence on the temperature is observed. The operating temperature of the target during data collection was 60 K.

uncertainties. In Fig. 16, a scan of the cell temperature down to very low temperatures is shown. The result indicates that no wall depolarization occurs. As a consequence, for the deuterium target the sampling correction for nuclear depolarization equals unity ($c_{\mathrm{P}} = 1$), so that

$$P_a = P_a^{\mathrm{BRP}}. \tag{60}$$

Moreover, the calculated depolarization due to spin exchange collisions resulted in $\Delta P_a^{se} = 0.3\%$. As in 2000 spin relaxation can be neglected completely, the polarization injected by the ABS equals the measured BRP value

$$P_a^{inj} \simeq P_a^{BRP}. \tag{61}$$

The polarizations measured by the BRP were found to be consistent with those calculated as described in Section 5.3, within the uncertainties.

6.2.2. Recombination

Although atomic recombination depends strongly on temperature, no variation of the measured atomic fraction α^{TGA} over a very wide temperature range around the working temperature $T_{cell} = 60\,K$ was ever observed during the whole year. Fig. 17 (upper plot) reports a cell temperature scan performed in August. (For

comparison a temperature scan performed with hydrogen in 1997 is also shown in the lower plot of the same figure). Additionally the measurement of the fraction α_r^{TGA} of atoms surviving recombination yielded the following average value:

$$\alpha_r^{TGA} = 0.997 \pm 0.014 \tag{62}$$

confirming that within the measured uncertainty no evidence of recombination was found. Therefore, for the deuterium operating period in 2000, both the deviation from unity of the sampling correction c_α, and the impact of the uncertainty in β are negligible.

6.3. Transverse hydrogen running in 2002

During the 2002–2003 operating period, the HERMES transversely polarized hydrogen target worked in a very stable way. On the other hand,
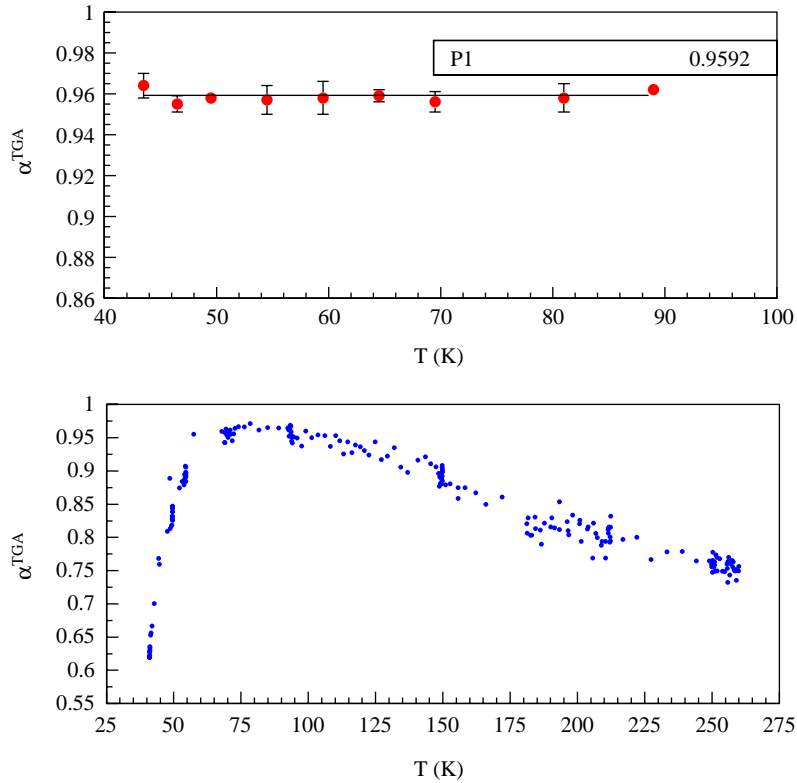
Fig. 17. Upper plot: measured atomic fraction as a function of the cell temperature for $T_{cell} < 100\,K$ for the deuterium running in 2000. No dependence on the temperature can be seen. The working temperature during normal operation was set to $T_{cell} = 60\,K$. For comparison a temperature scan with hydrogen taken in 1997 is shown in the lower plot.

the poor performance of the HERA beam did not allow a detailed study of the bunch induced depolarization. Nevertheless, by scanning the target magnetic field a working field value was established where the loss of polarization due to the field non-uniformity was limited to 1.5 % at the highest available beam currents (25 mA). The average target polarization $(P_{z+} - P_{z-})/2$ during the 2002 data taking period was 0.783 ± 0.041. This value is lower than that reported for the longitudinal hydrogen target (Section 6.1), mainly due to the lower applied target holding field and to the fact that the higher density allowed by the use of the intermediate size cell resulted in an increase of spin relaxation due to spin exchange collisions.

The stability of the transverse target operation during the 2002 running period is illustrated

in Fig. 18. The target density in this period measured via spin-exchange collisions was 1.1×10^{14} nucl./cm^2.

7. Discussion

Table 8 summarizes averaged values for the target properties during the various running periods. A comparison between the longitudinally polarized hydrogen and deuterium target leads to the following conclusions. At the same guide field, in the case of deuterium the spin exchange and wall relaxation processes are suppressed by a factor $(B_C^H/B_C^D)^2 \simeq 20$ compared to hydrogen. The positive and negative P_z values for hydrogen coincide very well, while for deuterium there is a
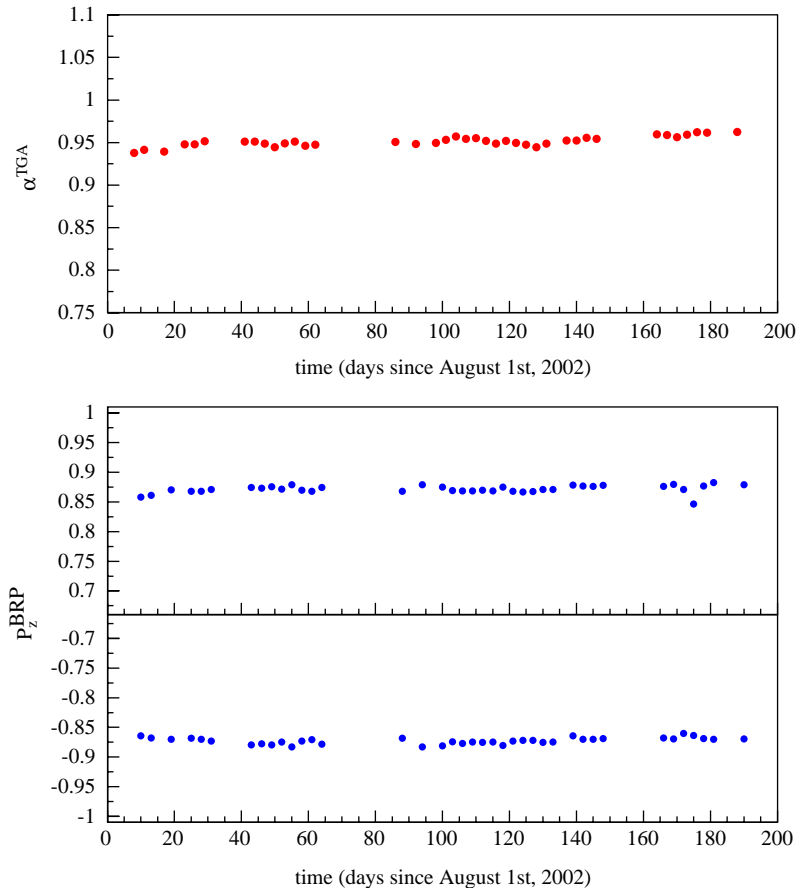

Fig. 18. The TGA (above) and BRP (below) measurements for the 2002/03 data taking period.

Table 8
Summary of the HERMES target performance in the years 1997, 2000 and 2002

	$H_{\parallel}(1997)$	$H_{\perp}(2002)$	$D_{\parallel}(2000)$
α_0	0.960 ± 0.010	0.918 ± 0.032	0.919 ± 0.026
α_r	0.945 ± 0.035	0.979 ± 0.023	0.997 ± 0.017
P_{z+}	$+0.908 \pm 0.016$	$+0.859 \pm 0.032$	$+0.927 \pm 0.017$
P_{z-}	-0.908 ± 0.016	-0.859 ± 0.032	-0.915 ± 0.010
$-\Delta P_{SE}$	0.035	0.055	$\leqslant 0.001$
$-\Delta P_{WD}$	0.02	0.055	$\leqslant 0.01$
$-\Delta P_{BI}$	Absent	0.015	Absent
P_+	$+0.851 \pm 0.031$	$+0.783 \pm 0.041$	$+0.851 \pm 0.029$
P_-	-0.851 ± 0.031	-0.783 ± 0.041	-0.840 ± 0.026
t (10^{14} nucleons/cm^2)	0.7	1.1	2.1
FOM ($P^2 t$) (10^{14}/cm^2)	0.5	0.67	1.5

The tabulated values are averaged over the respective running periods. The ΔP_i's represent the polarization losses arising from the listed process (see text).

clear difference. This is due to the larger number of efficiencies and transmissions involved.

From the table it is possible to deduce departures from the optimal performance like the amount of recombination ($\Delta \alpha_r = 1 - \alpha_r$), and the depolarization due to the various depolarizing mechansims: spin-exchange collisions (ΔP_{SE}), wall-depolarization (ΔP_{WD}) and beam-induced fields (ΔP_{BI}). The target density integrated over the cell length, or areal density t, is also shown together with a relative factor of merit (FOM) that takes into account both the polarization and the density. It is worthwhile to mention again that in 1997 the target cell had a larger cross-section ($29\,\text{mm} \times 9.8\,\text{mm}$) implying a higher conductance and a correspondingly lower density (about 40 %). The table also illustrates once more the optimal performance of the $D_{\parallel}$ target in 2000. For this target no recombination ($\Delta \alpha_r = 0$) and no depolarization phenomena ($\Delta P_{WD} = \Delta P_{SE} = \Delta P_{BI} = 0$) have been observed. This excellent behavior has to be attributed to the lower critical field of deuterium ($11.7\,\text{mT}$) compared to hydrogen ($50.7\,\text{mT}$), and to an improvement in the knowledge and preparation of the cell surface coating. The improved surface coating is also responsible for the better performance of the 2002 $H_{\perp}$ target compared to the 1997 $H_{\parallel}$ target, as far as the amount of recombination is concerned.

On the other hand, in 2002, due to the higher density obtained and the higher number of wall collisions, spin-relaxation effects became more important, causing a loss in polarization of about 11 % and limiting the gain in the factor of merit with respect to the 1997 running due to the increase in density. This indicates how an enhancement in the figure of merit of the target might be obtained by increasing the holding field proportionally with the density, in order to limit the spin relaxation effects.

8. Selected HERMES results

In this last section before the conclusions, some of the measurements which have been carried out at HERMES with the polarized internal gaseous target during the various running periods are mentioned. The number of deeply inelastic scattering events (after data quality selection) collected with the three polarized targets is given in Table 9.

Among the measurements which have been performed using the HERMES detector, we quote the following few: the measurement of the g_1^p structure function [34]; the measurement of the g_1^d structure function [35]; the first measurement of the b_1^d structure function [36]; measurements of the quark-flavour decomposition of the nucleon spin [37,38]; the first measurements of single-spin asymmetries in deep-inelastic scattering off both longitudinal and transversely polarized targets

Table 9
Deeply inelastic scattering events collected with the three polarized targets after data quality selection

Target (year)	DIS/million
$H_\parallel (1996-97)$	2.4
$D_\parallel (1998-2000)$	9.1
$H_\perp (2002-03)$	0.7

The numbers are given in millions.

[39–41] and a first study of the gluon polarization in nucleons [42].

9. Conclusion

The HERMES polarized hydrogen/deuterium target has been reliably operating since 1996. It provides polarization values between 0.78 and 0.85, densities $1-2 \times 10^{14}$ nucleons/cm^2, and total systematic uncertainties of only 0.03–0.04. The systematics of both the recombination and depolarization processes in the storage cell are fully under control.

References

[1] HERMES Technical Design Report, DESY-PRC 93/06, 1993.
[2] K. Rith, Progr. Part. Nucl. Phys. 49 (2002) 245.
[3] A.A. Sokolov, I.M. Ternov, Sov. Phys. Doklady 8 (1964) 1203.
[4] D.P. Barber, et al., Phys. Lett. B 343 (1995) 436.
[5] K. Ackerstaff, et al., Nucl. Instr. and Meth. A 417 (1998) 230.
[6] E. Steffens, W. Haeberli, Rep. Prog. Phys. 66 (2003) 1887.
[7] A. Nass, et al., Nucl. Instr. and Meth. A 505 (2003) 633.
[8] C. Baumgarten, et al., Nucl. Instr. and Meth. A 496 (2003) 277.
[9] C. Baumgarten, et al., Nucl. Instr. and Meth. A 508 (2003) 268.
[10] C. Baumgarten, et al., Nucl. Instr. and Meth. A 82 (2002) 606.
[11] C. Baumgarten, et al., Nucl. Instr. and Meth. A 496 (2003) 263.
[12] K. Ackerstaff, et al., Phys. Rev. Lett. 82 (1999) 1164.
[13] A. Airapetian, et al., Eur. Phys. J. D 29 (2004) 21.
[14] C. Baumgarten, et al., Eur. Phys. J. D 18 (2002) 37.
[15] C. Baumgarten, Ph.D. Thesis, University of Munich, Germany, DESY-THESIS-2000-038 (2000).
[16] G.E. Thomas, et al., Nucl. Instr. and Meth. A 257 (1987) 32.
[17] M.A. Bouchiat, J. Phys. Radium 24 (1963) 379.
[18] M.A. Bouchiat, J. Phys. Radium 24 (1963) 611.
[19] M.A. Bouchiat, J. Brossel, Phys. Rev. 147 (1965) 41.
[20] P.W. Anderson, in: G.T. Radio, H. Suhl (Eds.), Magnetism, vol. I, Academic Press, N.Y. (1963).
[21] N. Koch, E. Steffens, Rev. Sci. Instrum. 70 (1999) 1631.
[22] K. Halbach, Nucl. Instr. and Meth. A 169 (1980) 213.
[23] D. Reggiani, Ph.D. Thesis, University of Ferrara, Italy, DESY-THESIS-2003-001, 2003.
[24] S. Holloway, Surf. Sci. 299/300 (1994) 656.
[25] B. Braun, Ph.D Thesis MPIH-V25, Ludwig Maximilians-University, Munich, Germany, 1995.
[26] J.S. Price, W. Haeberli, Nucl. Instr. and Meth. A 326 (1993) 416.
[27] J.S. Price, W. Haeberli, Nucl. Instr. and Meth. A 349 (1994) 321.
[28] H. Kolster, Ph.D. Thesis, Ludwig Maximilians-University, Munich, Germany, 1998.
[29] E.M. Purcell, G.B. Fields, Astrophys. J. 124 (1956) 542.
[30] M. Desainfuscien, C. Auodoin, Phys. Rev. A 13 (1976) 2070.
[31] A.C. Allison, Phys. Rev. A 5 (1972) 2695.
[32] J.F.J. van den Brand, et al., Phys. Rev. Lett. 78 (1997) 1235.
[33] T. Wise, et al., Phys. Rev. Lett. 87 (2001) 042701.

[34] A. Airapetian, et al., Phys. Lett. B 442 (1998) 484.

[35] C. Weiskopf, Proceedings of the IX International Conference on Deep Inelastic Scattering and QCD (DIS 2001), Bologna, Italy, 2001.

[36] M. Contalbrigo, Proceedings of XV International Spin Physics Symposium (SPIN 2002), Brookhaven National Laboratory-NY (USA), 2002.

[37] K. Ackerstaff, et al., Phys. Lett. B 464 (1999) 123.

[38] A. Airapetian, et al., Phys. Rev. Lett. 92 (2004) 012005.

[39] A. Airapetian, et al., Phys. Rev. Lett. 84 (2000) 4047.

[40] A. Airapetian, et al., Phys. Rev. B 562 (2003) 182.

[41] A. Airapetian, et al., Phys. Rev. Lett.; hep-ex/0408013, submitted for publication.

[42] A. Airapetian, et al., Phys. Rev. Lett. 84 (2000) 2584.